**Title**

# Myelination-dependent mitochondria clustering and calcium buffering in parvalbumin interneuron axons

**Authors**

Koen Kole[1]*, Bas J. B. Voesenek[1], Maria E. Brinia[1,3], Naomi Petersen[1] and Maarten H. P. Kole[1,2]*

* Corresponding authors emails: k.kole@nin.knaw.nl and m.kole@nin.knaw.nl

**Affiliations**

[1] Axonal Signaling Group, Netherlands Institute for Neuroscience, Royal Academy of Arts and Sciences, Meibergdreef 47, 1105 BA, Amsterdam, the Netherlands

[2] Cell Biology, Neurobiology and Biophysics, Department of Biology, Faculty of Science, Utrecht University, Padualaan 8, 3584 CH, Utrecht, the Netherlands

[3] Medical School, National Kapodistrian University of Athens, Athens 11527, Greece

**Abstract**

Parvalbumin-expressing ($PV^+$) interneurons are fast-spiking cells that exert critical control over local neuronal circuit activity and oscillations. While it is well established that axons of $PV^+$ interneurons are myelinated its role remains poorly understood. One leading hypothesis is that myelin provides trophic support to sustain the metabolic demands of high-frequency spike generation of $PV^+$ interneurons. Here we developed Cre-dependent AAV vectors enabling cell type-specific investigation of the distribution and functional properties of mitochondria using genetically encoded fluorescent probes. Patch-clamp recordings followed by single-cell reconstructions revealed that mitochondria cluster to myelinated segments of $PV^+$ axons, which was lost upon experimental demyelination. Furthermore, two-photon imaging of action potential-evoked mitochondrial calcium (mt-$Ca^{2+}$) responses revealed high mt-$Ca^{2+}$ in unmyelinated segments and branch points compared to myelinated internodes. In contrast, demyelination caused uniform low mt-$Ca^{2+}$ responses. Together, these results suggest that $PV^+$ myelination regulates localization of mitochondria and activity-dependent local metabolic demands in axons.

48 **MAIN TEXT**

49

50 **Introduction**

51 In the vertebrate central nervous system, oligodendrocytes wrap multilamellar membranes
52 around axons to form myelin sheaths, which reduce local internodal depolarization, speed up action
53 potential propagation and enhance action potential fidelity (Nave and Werner, 2014; Cohen et al.,
54 2020). Although the myelin sheath strongly facilitates the electrical conductivity of internodes, its
55 insulation also prevents the axolemma from taking up glucose and other metabolites from the
56 extracellular space. Glycolytic oligodendrocytes aid neurons in overcoming this hurdle by
57 providing trophic support to the axon via the myelin sheath in the form of pyruvate and lactate
58 (Fünfschilling et al., 2012; Lee et al., 2012). Oligodendrocyte-axon metabolic coupling fuels in
59 particular axonal mitochondria, versatile organelles that are chiefly committed to the production of
60 adenosine triphosphate (ATP). Previous research, mostly performed in glutamatergic axons,
61 showed the critical role of such metabolic support for preserving mitochondrial integrity. The loss
62 of myelin is associated with dysfunction and shape changes of axonal mitochondria in both multiple
63 sclerosis (MS; Mahad et al., 2009; Witte et al., 2009; Zambonin et al., 2011) and demyelination
64 models (Kiryu-Seo et al., 2010; Nikic et al., 2011; Ohno et al., 2014; Licht-Mayer et al., 2020). For
65 example, typically the mitochondrial size and density increase together with electron transport
66 chain protein expression, and mitochondria lose their membrane potential which is critical for ATP
67 synthesis (Witte et al., 2009; Nikic et al., 2011; Zambonin et al., 2011).

68 Myelination is not limited to excitatory axons but is also found around inhibitory
69 GABAergic axons, nearly exclusively those belonging to parvalbumin-expressing interneurons
70 ($PV^+$ interneurons; Micheva et al., 2016; Stedehouder et al., 2017; Dubey et al., 2022). Comprising
71 the most abundant interneuron cell type in the cortex, $PV^+$ interneurons are characterized by highly
72 complex and extensive axonal organization enabling critical control of the local circuitry and
73 control over gamma oscillations (Hu et al., 2014; Kepecs and Fishell, 2014). $PV^+$ interneurons
74 possess small diameter axons (~0.4 µm, Stedehouder et al., 2019) which could make them highly
75 vulnerable to pathology of the myelin sheath (Evangelou et al., 2001; Edgar et al., 2009). We
76 recently found that experimental demyelination through toxic or genetic means critically disrupts
77 inhibitory transmission by $PV^+$ interneurons, characterized by fewer presynaptic terminals, reduced
78 intrinsic excitability and an abolishment of gamma oscillations (Ramaglia et al., 2021; Dubey et
79 al., 2022). In line with these findings, recent work shows that MS is associated with a specific loss
80 in $PV^+$ interneurons and $PV^+$ presynaptic terminals (Dutta et al., 2006; Ramaglia et al., 2021; Zoupi
81 et al., 2021). Whether the myelin sheaths of $PV^+$ axons play a role in the metabolic supply is not

82 well understood. One frequently raised hypothesis is that $PV^+$ myelination provides trophic support
83 to axonal mitochondria to maintain their very high levels of spike generation and activity during
84 gamma oscillations (Micheva et al., 2016, 2018; Stedehouder and Kushner, 2017). With a low
85 threshold of action potential generation, sustained high firing frequencies and synchronization with
86 fast gamma oscillations, $PV^+$ interneurons use large amounts of energy to fuel the
87 sodium/potassium ATPase activity to maintain the balance of ionic gradients (Li et al., 2014; Hu et
88 al., 2018). In line with their high energy usage, $PV^+$ interneurons are indeed characterized by a
89 relatively high mitochondrial content and cytochrome C oxidase (Kageyama and Wong-Riley,
90 1982; Kann et al., 2014) and deficits in the spatial distribution of mitochondria in $PV^+$ axons are
91 associated with impairments of gamma oscillations (Kontou et al., 2021).
92 To directly examine how myelination affects mitochondria distribution and function we
93 developed a Cre-dependent viral approach to express mitochondria-targeted genetically encoded
94 fluorescent reporters, mt-GFP and mt-GCamp6f in Cre-driver lines, enabling the study of
95 mitochondrial distribution and $Ca^{2+}$-buffering properties, respectively. Two-photon guided patch-
96 clamp recordings from $PV^+$ interneurons of the somatosensory cortex followed by confocal
97 microscopy and reconstructions with submicron precision revealed that in normally myelinated
98 axons mt-GFP signals are clustered to myelinated segments of $PV^+$ axons, which was disrupted
99 following experimental demyelination. In addition, two-photon imaging of action potential-evoked
100 mitochondrial $Ca^{2+}$ transients (mt-GCamp6f) showed that mitochondria near the branch points and
101 nodes of Ranvier produced high $Ca^{2+}$ buffering activity, which attenuated following demyelination.
102 These results indicate that in neocortical $PV^+$ interneuron axons myelination spatially organizes
103 mitochondria, locally increasing the mitochondrial content within internodes and increases
104 mitochondrial $Ca^{2+}$ buffering at branch points, revealing a novel axoglial mechanism to increase
105 axonal branch diversification and direct metabolic supply to sites with high energy demands.
106
107

## Results

*An AAV-mediated approach for cell type-specific labeling of mitochondria*

We first developed a Cre-dependent adeno-associated viral (AAV) vector (AAV-EF1a-mt-GFP-DIO; **Figure 1A**) and examined the *in vivo* mitochondrial labeling. The use of an AAV vector allowed control over transduction rates to enable single-cell analyses, an important advantage over brain-wide cell type-specific expression (Fecher et al., 2019). Upon injection into the somatosensory cortex (S1) of Cre-expressing transgenic mice (**Figure 1B**), this viral vector results in GFP-labeled mitochondria with high cell type specificity (**Figure 1C-G**). Consistent with the known location of $PV^+$ interneurons *in vivo*, expression of mt-GFP-DIO in PV-Cre; Ai14 mice in which $PV^+$ interneurons are labelled with the red fluorescent protein tdTomato labelled neurons across cortical layers 2 to 6 (**Figure 1C**; Meyer et al., 2011). We quantified the overlap between mt-GFP and tdTomato in PV-Cre; Ai14 mice and found a high cell type specificity (~98%; **Figure 1D**). Furthermore, two-photon-guided targeted whole-cell recordings from mt-GFP-expressing (mt-$GFP^+$) cells corroborated this cell type-specificity. All mt-$GFP^+$ cells fired action potentials at high frequency (123.41 ± 13.13 Hz upon 500 pA current injection; $n$ = 8 cells from 5 mice). Their action potentials were brief in half-width (295.74 ± 2.52 µs; $n$ = 5 cells from 4 mice) and showed a prominent afterhyperpolarization (−15.83 ± 2.25 mV; $n$ = 5 cells from 4 mice, **Figure 1E**), consistent with previously described properties of neocortical $PV^+$ interneurons (Li et al., 2014).

To further examine the Cre dependency of *in vivo* mt-GFP-DIO AAV vector, we expressed mt-$GFP^+$ in Rbp4-Cre mice, a Cre-driver line commonly used to label cortical layer (L)5 pyramidal neurons (PNs) (Gerfen et al., 2013). In Rbp4-Cre mice, mt-$GFP^+$ somata were pyramidally shaped, restricted to L5 and possessed a prominent apical dendrite, which are characteristic of L5 PNs (**Figure 1F**; Hamada et al., 2016). Mt-$GFP^+$ cells in Rbp4-Cre mice always discharged action potentials in low-frequency trains (40.45 ± 4.76 Hz upon 500 pA current injection; $n$ = 13 cells from 4 mice) and of comparatively large width (680.85 ± 15.80 µs; $n$ = 11 cells from 4 mice), consistent with the known electrophysiological properties of L5 pyramidal neurons (**Figure 1G**; ref(Hamada and Kole, 2015). Mitochondria are motile organelles but are substantially more stationary in adult mice and *in vivo* (Smit-Rigter et al., 2016). We quantified mitochondrial motility in a subset of our mt-$GFP^+$ acutely prepared slices and found that the vast majority (~99%) of mitochondria were stable in both cell types (**Supplementary Figure 1**). Together, these findings indicate that mt-GFP-DIO enables the study of mitochondria in a highly cell-type specific manner.

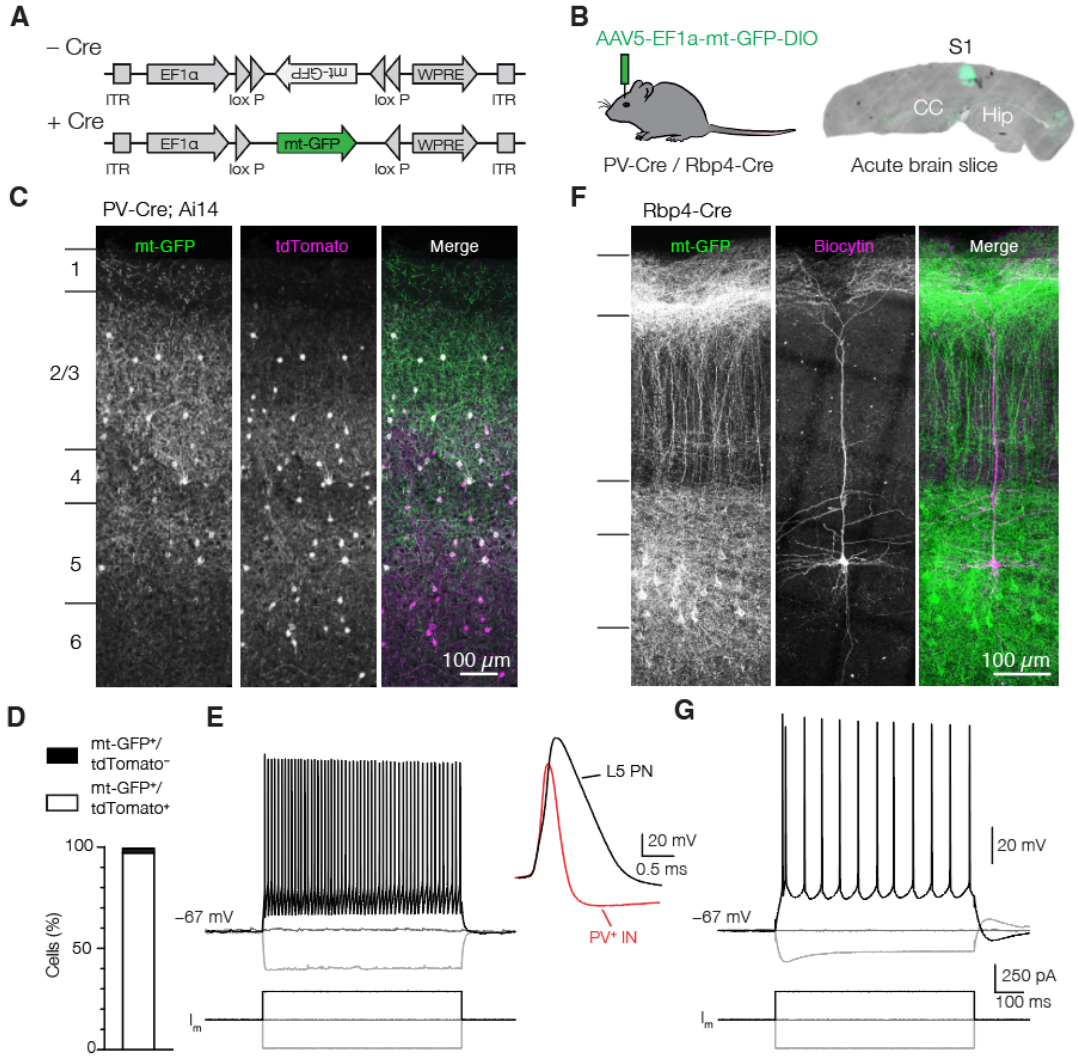


**Figure 1 – mt-GFP expresses selectively in a Cre-dependent and cell-type-specific manner. A** Schematic of the AAV construct design. Mitochondria-targeted green fluorescent protein (mt-GFP) requires Cre recombination for expression under the EF1α promoter. **B** PV-Cre; Ai14 or Rbp4-Cre mice were injected with AAV5-EF1a-mt-GFP-DIO. CC, corpus callosum; Hip, hippocampus. **C** Expression in PV-Cre; Ai14 mice results in high overlap between tdTomato and mt-GFP. **D** Quantification of mt-GFP and tdTomato overlap. 243/248 cells or 97.94% of mt-GFP$^+$ cells are also tdTomato$^+$; $n$ = 248 cells in 7 sections from 2 mice. **E** Example traces of action potentials in a mt-GFP$^+$ fast spiking PV$^+$ interneuron. Inset shows single action potentials in mt-GFP$^+$ cells from a PV-Cre; Ai14 or Rbp4-Cre mouse (aligned at onset). **F** AAV expression in Rbp4-Cre mice results in mitochondrial labeling in L5 pyramidal neurons. Note the characteristic apical dendrites visualized by mt-GFP. **G** Example traces of an action potential train in mt-GFP$^+$ L5 PN.

*Mitochondria are clustered at the axonal initial segment (AIS) and enlarged upon demyelination*

To examine the contribution of myelination to mitochondria distribution we injected PV-Cre; Ai4 mice with AAV-EF1a-mt-GFP-DIO in S1 and fed mice either with control food or a diet supplemented with 0.2% cuprizone, which selectively kills oligodendrocytes, leading to widespread cortical demyelination (Kipp et al., 2009).

59 We first focused on the axon initial segment (AIS), a highly excitable domain at the base of
60 the axon where action potentials (APs) are initiated and which is known to respond to demyelination
61 (Kole et al., 2007; Hamada and Kole, 2015). The AIS was identified by immunostaining for the
62 anchoring protein βIV spectrin in cortical tissue from mt-GFP-expressing PV-Cre; Ai14 mice. By
63 contouring of the perimeter of mt-GFP signals we subsequently estimated the shape and size of
64 mitochondria. The results showed that in both control and cuprizone-treated mice, mitochondria
65 density was high in the AIS and gradually reduced with distance from the soma (two-way ANOVA;
66 distance effect $P < 0.0001$; **Figure 2A**, **Supplementary Figure 2A**). This distribution was
67 unchanged in cuprizone-treated mice (two-way ANOVA; interaction effect treatment × distance, $P$
68 $= 0.7841$). However, the mitochondrial area was significantly increased in axons from cuprizone-
69 treated mice (nested t-test, $P = 0.0241$; **Figure 2A-C**). In contrast, the mitochondrial form factor
70 and density were unaffected (**Figure 2D, E**).
71 Both the AIS length and onset relative to the soma were comparable between groups
72 (unpaired t-test, $P = 0.2112$ and $P = 0.6055$, respectively; **Figure 2F-G**). AIS length and location
73 are critical to the current threshold for AP generation (Kole and Brette, 2018). To test whether AP
74 initiation is indeed preserved we performed whole-cell recordings from $PV^+$ interneurons in acute
75 slices. In all slice experiments, we recorded features of excitability in artificial cerebral spinal fluid
76 containing 5 mM L-lactate and 10 mM D-glucose to more closely resembling the *in vivo*
77 extracellular environment. In accordance with the unaffected anatomical properties of the AIS,
78 electrophysiological recordings of $PV^+$ interneurons revealed no change in AP wave form, voltage
79 or current threshold, amplitude, half-width, or resting membrane potential (**Figure 2H-I**;
80 **Supplementary Figure 2B-F**). However, demyelinated $PV^+$ interneurons displayed a higher
81 rheobase (**Figure 2J**) and a lower input resistance (**Figure 2K**) and lower firing rate upon sustained
82 somatic current injection (two-way ANOVA; treatment effect $P = 0.0304$; **Figure 2L-M**),
83 indicating reduced excitability, in line with previous recordings of demyelinated $PV^+$ basket cell
84 interneurons (Dubey et al., 2022). Together, these results show that mitochondria are enriched at
85 the AIS and are larger in size following demyelination.
86

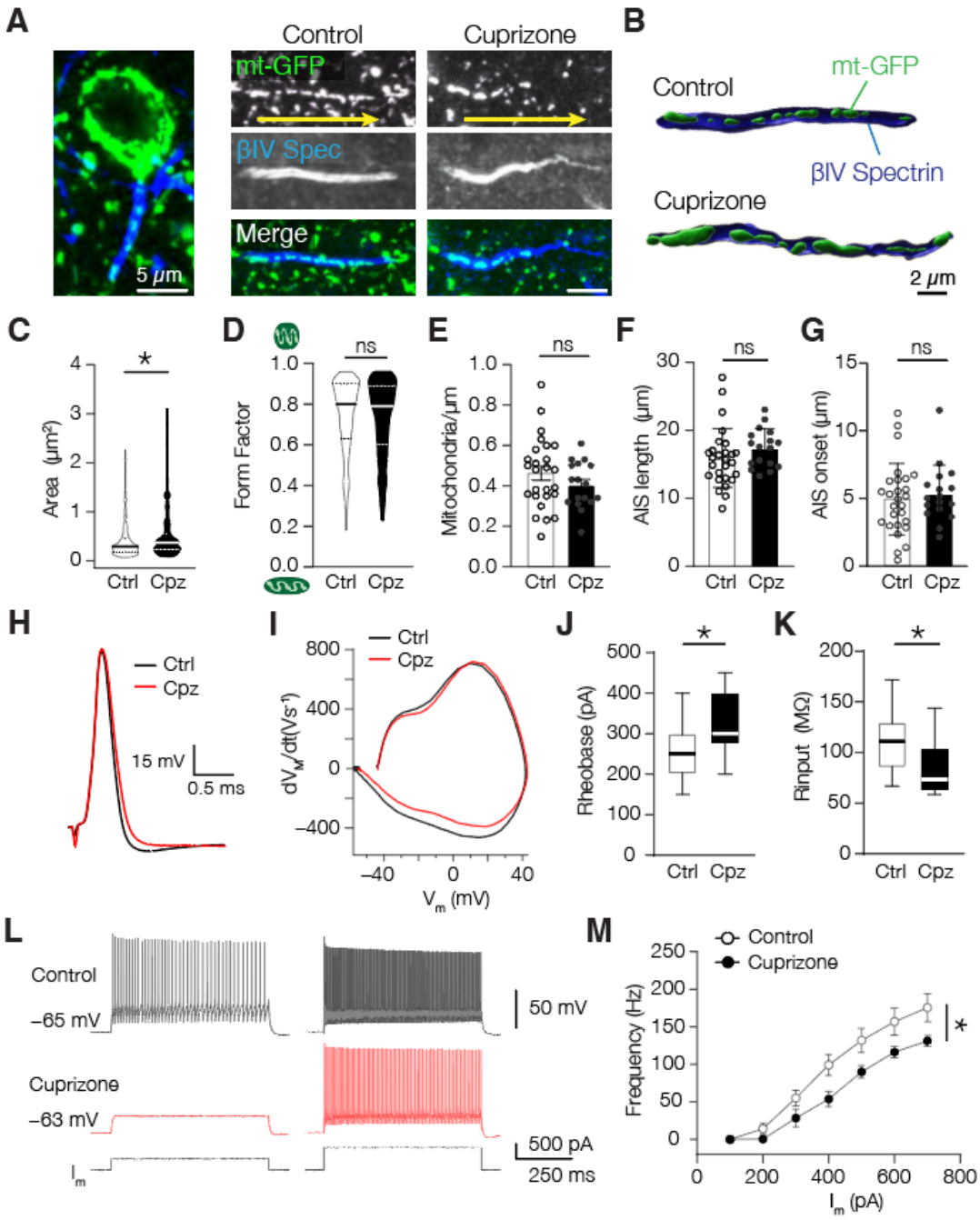


**Figure 2 – Cuprizone-induced demyelination enlarges AIS mitochondria and reduces PV⁺ interneuron excitability** **A** Example images of mitochondria (green) at the AIS (blue) of PV⁺ interneurons. Arrows (yellow) indicate anterograde direction of the axon. **B** 3D surface rendering of PV⁺ AISs containing mitochondria of control or cuprizone-treated axons. **C** Mitochondrial area is increased upon demyelination (nested t-test, **P* = 0.0241; df = 43; control, *n* = 215 mitochondria in 27 AISs from 4 mice; cuprizone, *n* = 144 mitochondria in 18 AISs from 3 mice). **D** Mitochondrial form factor is unaffected (nested t-test, *P* = 0.6876; df = 43; control, *n* = 215 mitochondria in 27 AISs from 4 mice; cuprizone, *n* = 144 mitochondria in 18 AISs from 3 mice). **E** Density of AIS mitochondria are unchanged upon demyelination (unpaired t-test, *P* = 0.2396; df = 41; control, *n* = 27 AISs from 4 mice; cuprizone, *n* = 17 AISs from 3 mice). **F** AIS length is unaffected by cuprizone-treatment (unpaired t-test, *P* = 0.2112; df = 0.42; control, *n* = 27 AISs from 4 mice; cuprizone, *n* = 17 AISs from 3 mice). **G** AIS onset (soma edge to AIS) is comparable between control and

cuprizone-treated groups (unpaired t-test, $P = 0.6055$; df = 42; control, $n = 27$ AISs from 4 mice; cuprizone, $n = 17$ AISs from 3 mice). **H** Example single APs of a control and demyelinated $PV^+$ interneuron upon a 3 ms current injection. **I** Phase plots of the traces shown in d; Reduced $PV^+$ interneuron excitability suggested by **J** increased rheobase (unpaired t-test, $*P = 0.0104$; df = 33; control, $n = 22$ cells from 12 mice; cuprizone, $n = 13$ cells from 7 mice) and **K** reduced input resistance (unpaired t-test, $*P = 0.0337$; df = 33; control, $n = 22$ cells from 12 mice; cuprizone, $n = 13$ cells from 7 mice). **L** Example traces of $PV^+$ interneuron responses after control (black) or cuprizone (red) treatment in response to 400 (left) or 600 pA (right) current injection. **M** Reduced firing frequency upon somatic current injection in demyelinated $PV^+$ interneurons (two-way ANOVA with Bonferroni's post hoc test; interaction effect, $P = 0.0215$, $F_{(6, 126)} = 2.582$; treatment effect $*P = 0.0439$, $F_{(1, 21)} = 4.596$; control, $n = 17$ cells from 12 mice; cuprizone, $n = 11$ cells from 7 mice). Bar graphs (d-g) indicate the mean, individual data points represent cells, error bars indicate SEM; Box plots (j, k) represent the 25th to 75th percentiles, whiskers indicate the maximal and minimal values, solid line represents the median. In truncated violin plots (c, d), solid lines represent the median, dotted lines represent 25th and 75th quartiles.

*Mitochondria of the demyelinated $PV^+$ axon are increased in size and lost in proximal branches*

To examine the mitochondrial morphology and distribution within the extended cytoarchitecture of individual $PV^+$ interneurons we reconstructed mt-$GFP^+$ axons and dendrites of whole-cell recorded biocytin-filled $PV^+$ interneurons (**Figure 3A–E**). Axonal mitochondria in $PV^+$ interneurons were often found at branch points and *en passant* boutons and were smaller compared to their dendritic counterparts (**Figure 3C**; Cserep et al., 2018)). Quantification showed that compared to dendritic mitochondria those in axons covered less length (unpaired t-test, $P = 0.0093$, **Figure 3F**), were smaller (nested t-test, $P < 0.0001$; **Figure 3G**) and were more spherical (nested t-test, $P < 0.0001$; **Figure 3H**).

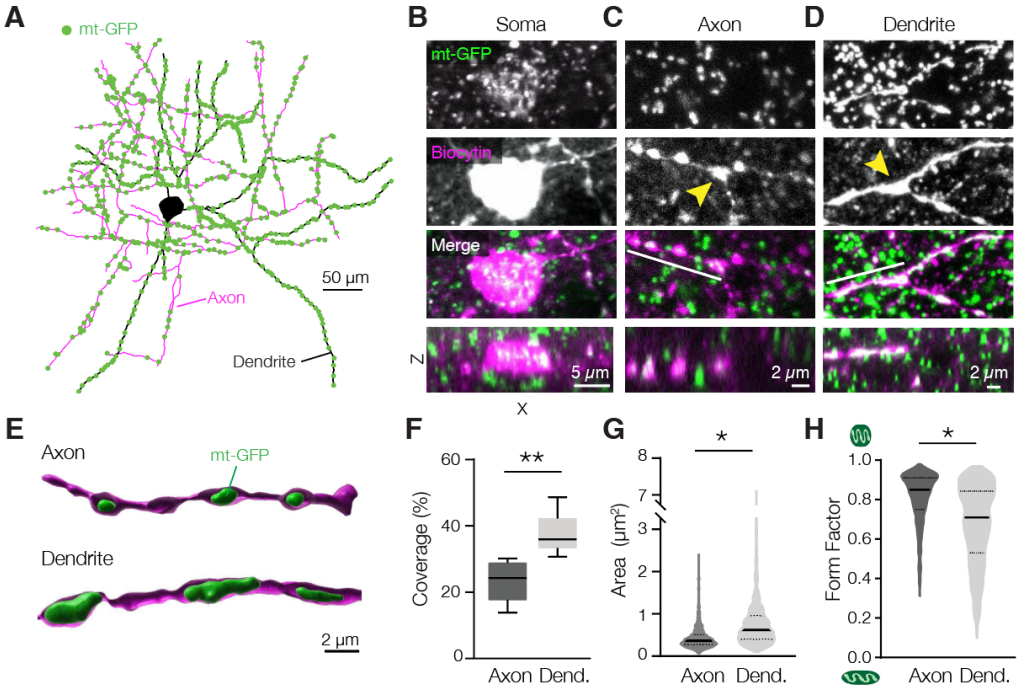


**Figure 3 – Axonal and dendritic PV$^+$ interneuron mitochondria are morphologically distinct.** **A** Example of a reconstructed PV$^+$ interneuron and the locations of its mitochondria (green). Magenta, axon; black, dendrite. Mitochondria in soma were not quantified. **B** Examples of somatic, **C** axonal and **D** dendritic mitochondria in PV$^+$ interneurons. Yellow arrowheads indicate branch points, white lines indicate axis used for *XZ* views. **E** 3D surface rendering of example axonal or dendritic mitochondria. **F** Percentage of PV$^+$ neurite length covered by mitochondrial length (unpaired t-test, $^{**}P = 0.0093$; df = 8; Axon, $n$ = 188 mitochondria; dendrite, $n$ = 482 mitochondria; 5 cells from 3 mice). **G** Area of mitochondria is larger in PV$^+$ dendrites (nested t-test, $^{*}P = 0.0144$; df = 8; Axon, $n$ = 859 mitochondria; dendrite, $n$ = 1138 mitochondria; 5 cells from 3 mice). **H** Form factor of mitochondria is lower in PV$^+$ dendrites, reflecting a more elongated morphology (nested t-test, $^{*}P = 0.0263$; df = 8; Axon, $n$ = 859 mitochondria; dendrite, $n$ = 1138 mitochondria; 5 cells from 3 mice). Box plots (f-h) represent the 25$^{th}$ to 75$^{th}$ percentiles, whiskers represent the maximal and minimal values, solid line represents the median. Solid lines in truncated violin plots represent the median, dotted lines represent 25$^{th}$ and 75$^{th}$ quartiles.

These anatomical differences between mitochondria are in agreement with previous findings in L2/3 (Lewis et al., 2018) and present findings in L5 pyramidal neurons (**Supplementary Figure 3**). Consistent with our observations at the AIS, demyelination significantly increased the size of axonal mitochondria (**Figure 4A, B**), with a mean surface area increase of ~60% (nested t-test, $P$ = 0.044; **Figure 4C**), without affecting mitochondrial shape (nested t-test, $P$ = 0.2776; **Figure 4D**), suggesting a uniform increase in mitochondrial size. Importantly, PV$^+$ interneuron myelination is most abundant at lower axonal branch orders (≤ 4$^{th}$ order; (Micheva et al., 2016; Stedehouder et al., 2017, 2019). To test whether demyelination affects axonal mitochondria in proximal branch orders differently compared to those in higher branch orders we separated the distal population from the 2$^{nd}$ to 4$^{th}$ branch orders and found that the demyelination-induced mitochondrial size increase was comparable (**Figure 4F**).

The PV axons did not show swellings or degradation and, consistent with previous work (Dubey et al., 2022), the total reconstructed axonal length was not different between control and demyelinated axons (unpaired t-test, P = 0.4918; **Figure 4G**). Interestingly however, quantification by branch order revealed an increased average segment length in proximal branches of demyelinated $PV^+$ axons (**Figure 4H**). The observation of local structural changes, together with findings showing that demyelination alters mitochondrial density (Witte et al., 2009; Zambonin et al., 2011; Licht-Mayer et al., 2020), prompted us to investigate the mitochondrial density in $PV^+$ axons. While the total mitochondrial density over all path lengths was comparable between control and demyelinated $PV^+$ axons (unpaired t-test, $P = 0.1170$; **Figure 4I**), mitochondria in the proximal branch orders of demyelinated axons were on average ~20% reduced in density (two-way ANOVA, branch order × treatment effect, $P = 0.0169$; **Figure 4J**). In higher branch orders (≥ 5) the mitochondria densities were similar between groups (two-way ANOVA with Bonferroni's post hoc test, $P > 0.9999$). In line with these observations, we found an increased inter-mitochondrial distance specifically in proximal branches of demyelinated axons (≤ $4^{th}$ order; Kruskal-Wallis test with Dunn's post hoc test, $P < 0.0001$; **Figure 4K**). Together, these results indicate that myelin loss results in a reduced mitochondrial clustering specifically in the proximal putatively demyelinated branches of the $PV^+$ axon.

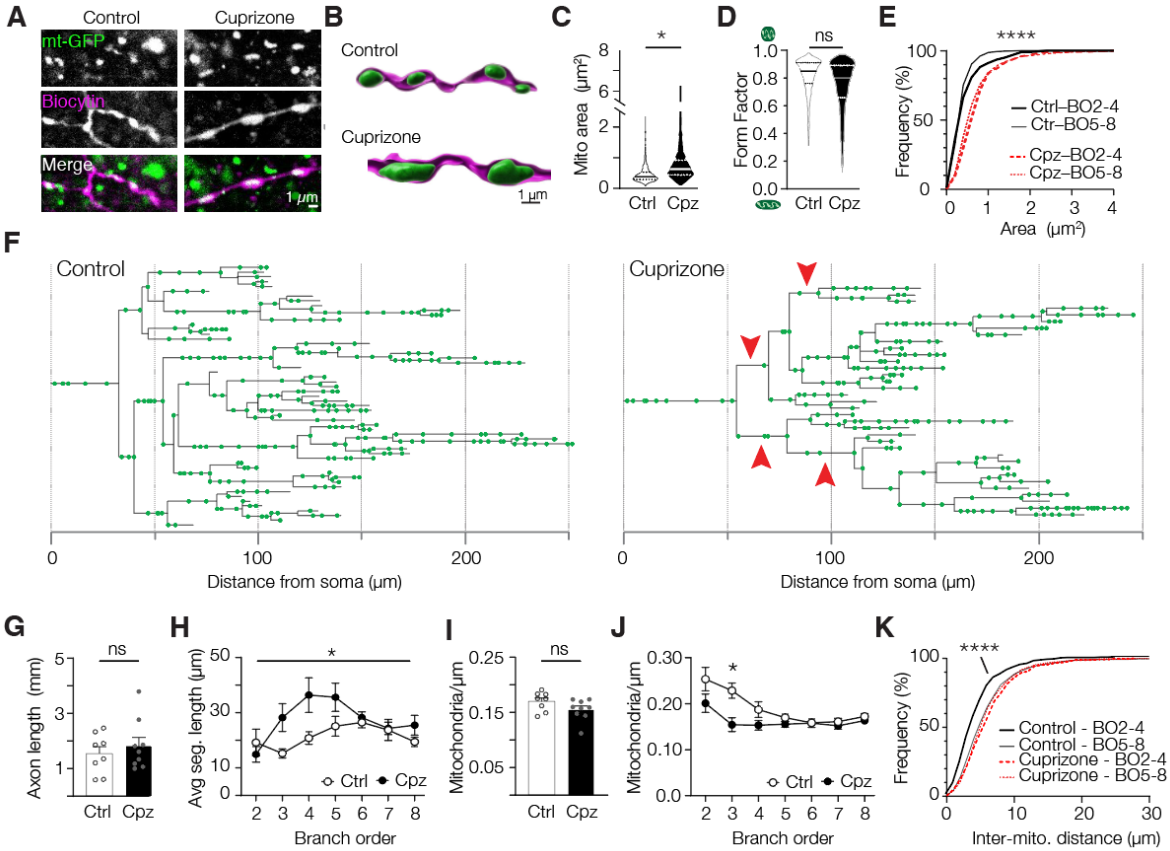


**Figure 4 – Cuprizone-induced demyelination reduces mitochondrial density in proximal axons.** **A** Example confocal images of mitochondria (mt-GFP) in control (left) and demyelinated axon (right). **B** 3D rendered images of mt-GFP and biocytin. **C** Increased mitochondrial size upon demyelination (nested t-test, *$P$ = 0.038; df = 8; control, $n$ = 5 axons, 805 mitochondria; 5 cells from 3 mice, same data as in Figure 2c-g. Cuprizone, $n$ = 5 axons, 1218 mitochondria; 5 cells from 4 mice). **D** Unchanged mitochondrial form factor in demyelinated axons (nested t-test, $P$ = 0.2776; df = 8; Control, $n$ = 5 axons, 805 mitochondria; 5 cells from 3 mice, same data as in Figure 2c-g; Cuprizone, $n$ = 5 axons, 1218 mitochondria; 5 cells from 4 mice). **E** Cumulative distribution plots of mitochondrial size showing uniform increase across all branch orders (BO, Kruskal-Wallis test ****$P$ < 0.0001; Dunn's post hoc test, All control vs cuprizone comparisons, $P$ < 0.0001, control BO 2-4 vs BO 5-8, $P$ = 0.8402; cuprizone BO 2-4 vs BO 5-8, $P$ = 0.3932. Control, $n$ = 5 axons, 805 mitochondria; 5 cells from 3 mice, same data as in Figure 2c-g. Cuprizone, $n$ = 5 axons, 1218 mitochondria; 5 cells from 4 mice). **F** Example axonograms of a control- (*left*) and a cuprizone-treated (*right*) $PV^+$ interneuron. Red arrowheads indicate examples of second, third or fourth branch orders where mitochondria appear relatively sparse. **G** Cuprizone treatment induces no change in axonal length (unpaired t-test, $P$ = 0.4918; df = 15; Control, $n$ = 8 axons, 5 mice; Cuprizone, $n$ = 9 axons, 5 mice). **H** Increased average segment length of demyelinated $PV^+$ axons (two-way ANOVA; branch order x treatment effect, *$P$ = 0.0440, $F_{(6,90)}$ = 2.266; branch order effect, $P$ = 0.0104, $F_{(3.916, 58.71)}$ = 3.660; treatment effect, $P$ = 0.0479, $F_{(1,15)}$ = 4.639; Bonferroni's post hoc test n.s.; Control, $n$ = 8 axons, 5 mice; Cuprizone, $n$ = 9 axons, 5 mice). **I** No change in overall axonal mitochondrial density (unpaired t-test, $P$ = 0.1170; df = 15; Control, $n$ = 8 axons, 5 mice; Cuprizone, $n$ = 9 axons, 5 mice). **J** Reduced mitochondrial density in early (<5) but no change in later branch orders upon demyelination (two-way ANOVA, Branch order x treatment effect, $P$ = 0.0169, $F_{(6,90)}$ = 2.747; branch order effect, $P$ < 0.0001, $F_{(2.764, 41.45)}$ = 9.560; treatment effect, $P$ = 0.0143, $F_{(1,15)}$ = 7.679; Bonferroni's post hoc test Branch order 3, *$P$ = 0.0340; Control, $n$ = 8 axons, 5 mice; Cuprizone, $n$ = 9 axons, 5 mice). **K** Increased distance between mitochondria in second to fourth branch orders of demyelinated axons but no change in later branch orders (Kruskal-Wallis test $P$ < 0.0001; Dunn's post hoc test, control vs cuprizone BO2-4, ****$P$ < 0.0001; control BO2-4 vs control BO5-8, $P$ < 0.0001; cuprizone BO2-4 vs cuprizone BO5-8, $P$ = 0.6008; Control, $n$ = 8 axons, 5 mice; Cuprizone,

$n$ = 9 axons, 5 mice). Solid lines in truncated violin plots (c, d) represent the median, dotted lines represent 25th and 75th quartiles. Bar graphs (g, i) represent the mean, individual data points represent axons, error bars represent SEM.

*Mitochondria are clustered at the myelinated PV$^+$ axon*

The loss of mitochondrial clustering in proximal axons following demyelination suggests that mitochondrial distribution is determined, at least in part, by the presence of the myelin sheath. If internode myelination is sufficient to cluster mitochondria this should be visible in the proximal axon arbors, which have diverse myelin patterns (Micheva et al., 2016; Stedehouder et al., 2017, 2019). To test this, we performed a triple staining for myelin basic protein (MBP), GFP and biocytin in sections from control mice and reconstructed PV$^+$ axons to quantify the mitochondrial density in MBP positive (MBP$^+$) and negative (MBP$^–$) axonal segments (**Figure 5A**). In agreement with previous findings (Stedehouder et al., 2017), MBP$^+$ segments were on average ~18 µm in length (range: 2.56–47.62 µm, $n$ = 32 internodes). Interestingly, axonal mitochondria in MBP$^+$ segments were larger compared to mitochondria in unmyelinated branches (nested t-test $P$ = 0.0121; **Figure 5B**), but not different in shape (nested t-test, $P$ = 0.1210; **Figure 5C**). Consistent with our hypothesis, MBP$^+$ axonal segments contained a significantly higher mitochondrial density compared to MBP$^–$ segments of the same axon and comparable branch orders (**Figure 5A, E)**. Furthermore, mitochondrial densities in control MBP$^–$ segments were not different from cuprizone-induced demyelinated PV$^+$ axons (**Figure 5A, D, E**). Together, these results support the idea that myelin wrapping clusters mitochondria locally within PV$^+$ internodes.

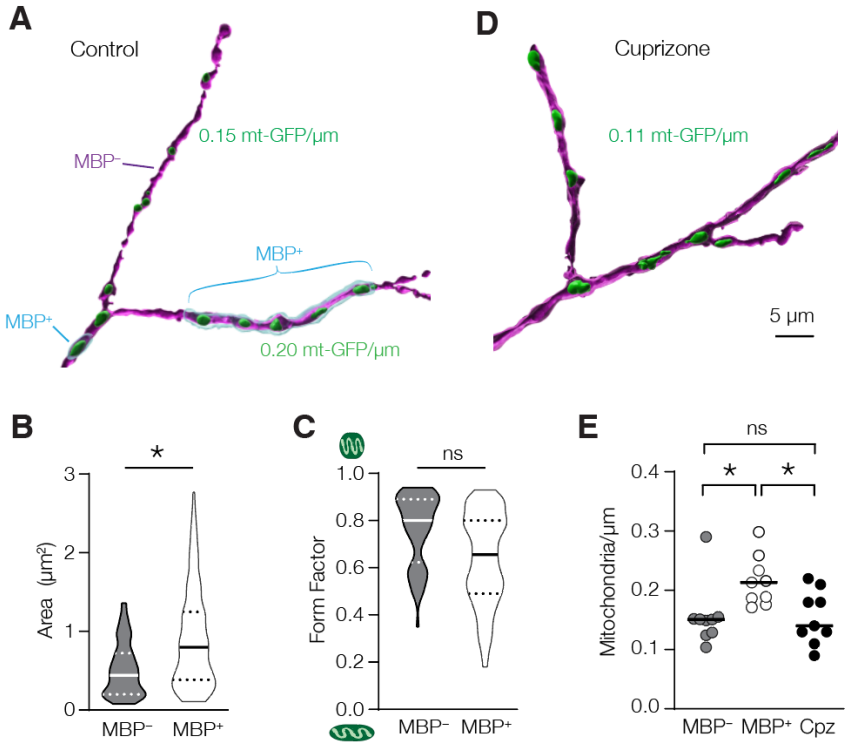


**Figure 5 – Mitochondria are clustered to the myelin sheaths of the PV$^+$ axon. A, D** 3D surface renderings of example regions of a control (A) or demyelinated (D) PV$^+$ axon. **B** Mitochondrial area is higher at the myelin sheath (nested t-test, $P = 0.0121$; df = 14; unmyelinated, $n = 68$ mitochondria; myelinated, $n = 114$ mitochondria, 8 axons from 6 mice). **C** Mitochondrial form factor is comparable between myelinated and unmyelinated axons (nested t-test, $P = 0.1210$; df = 14; unmyelinated, $n = 68$ mitochondria; myelinated, $n = 114$ mitochondria, 8 axons from 6 mice). **E** Mitochondrial density in the myelinated segment is higher compared to unmyelinated ones within the same axon (One-way ANOVA, $P = 0.0138$; Bonferroni's post hoc test, MBP$^-$ vs. MBP$^+$ $*P = 0.0356$, MBP$^+$ vs. cuprizone BO3 $*P = 0.0276$; MBP$^-$ vs cuprizone BO3 $P > 0.9999$; control, $n = 9$ axons from 6 mice; demyelinated, 9 axons from 5 mice, same data as Figure 4j). Solid lines in truncated violin plots (b, c) represent the median, dotted lines represent 25$^{th}$ and 75$^{th}$ quartiles. Solid bars in e represent the mean, individual data points represent axons.

*Demyelination disrupts mitochondrial $Ca^{2+}$ buffering in internodal segments*

Myelin loss is typically associated with increased mitochondrial content and increased axonal $Ca^{2+}$ influx, ultimately leading to cytoskeletal breakdown and axon degeneration (Campbell and Mahad, 2012; Witte et al., 2019). One pathway to control $Ca^{2+}$ accumulation in demyelination-induced pathology is through $Ca^{2+}$ buffering, a process which is also regulated by mitochondria (Rizzuto et al., 2012; Holman et al., 2020). To investigate mitochondrial $Ca^{2+}$ (mt-$Ca^{2+}$) uptake in PV$^+$ axons we employed AAV-mediated and Cre-dependent expression of the mitochondrion-targeted, genetically encoded calcium indicator mt-GCaMP6f in PV$^+$ interneurons (**Figure 6**). In acute slices of PV-Cre; Ai14 mice we targeted mt-GCaMP6f$^+$ PV$^+$ interneurons for whole-cell patch-clamp recordings and filled them with Atto594, revealing the cytoarchitecture (**Figure 6A**) and enabling targeted mitochondrial imaging. In the experiments we imaged mt-$Ca^{2+}$ fluorescence

59 responses following ~100 APs. In line with previous findings, we observed that during AP trains
60 mitochondria in the distal $PV^+$ axon showed strong $Ca^{2+}$ responses in putative *en passant* boutons,
61 clearly identifiable as varicosities along the thin axons, (**Supplementary Figure 4A-B**; Lewis et
62 al., 2018; Ashrafi et al., 2020). The amplitude of mt-$Ca^{2+}$ responses were comparable between
63 control and demyelinated axons (**Supplementary Figure 4B**). Similarly, we observed large
64 amplitude mt-$Ca^{2+}$ transients at the AIS of $PV^+$ interneurons, which were unchanged in amplitude
65 after demyelination (**Supplementary Figure 4C**). These findings suggest that activity-dependent
66 mt-$Ca^{2+}$ buffering in presynaptic terminals and the AIS of $PV^+$ interneurons is unaffected by myelin
67 loss.
68
69 To test whether there are differences in internodes, unmyelinated and/or demyelinated branches we
70 imaged mt-GCaMP6f along the proximal arbors ($\leq 5^{th}$ branch order) and subsequently
71 immunostained the slices for GFP, MBP and biocytin, allowing unequivocal assessment of the
72 location of mitochondria with respect to myelin sheaths (**Figure 6B-D**). We found that
73 mitochondria in normally myelinated axons showed AP-evoked $Ca^{2+}$ responses with greater
74 amplitudes within $MBP^-$ segments compared to those in internodes (Kruskal-Wallis test with
75 Dunn's post hoc test, $P < 0.0001$; **Figure 6D**). We next asked whether myelin loss would lead to
76 changes in mt-$Ca^{2+}$ buffering in demyelinated $PV^+$ interneurons. When we compared all mt-$Ca^{2+}$
77 responses in control axons (including both $MBP^+$ and $MBP^-$ segments) with those in putatively
78 demyelinated axons we found no difference between the two groups (nested t-test, $P = 0.6055$).
79 However, mt-$Ca^{2+}$ transients in cuprizone-treated axons were stronger compared to $MBP^+$ control
80 segments (Kruskal-Wallis test with Dunn's post hoc test, $P = 0.0039$; **Figure 6D)** and weaker
81 compared to $MBP^-$ segments (Kruskal-Wallis test with Dunn's post hoc test, $P = 0.0195$; **Figure**
82 **6D**). These results suggest that myelin dampens mt-$Ca^{2+}$ responses and that demyelination results
83 in a more uniform mt-$Ca^{2+}$ buffering profile in control $PV^+$ axons.
84

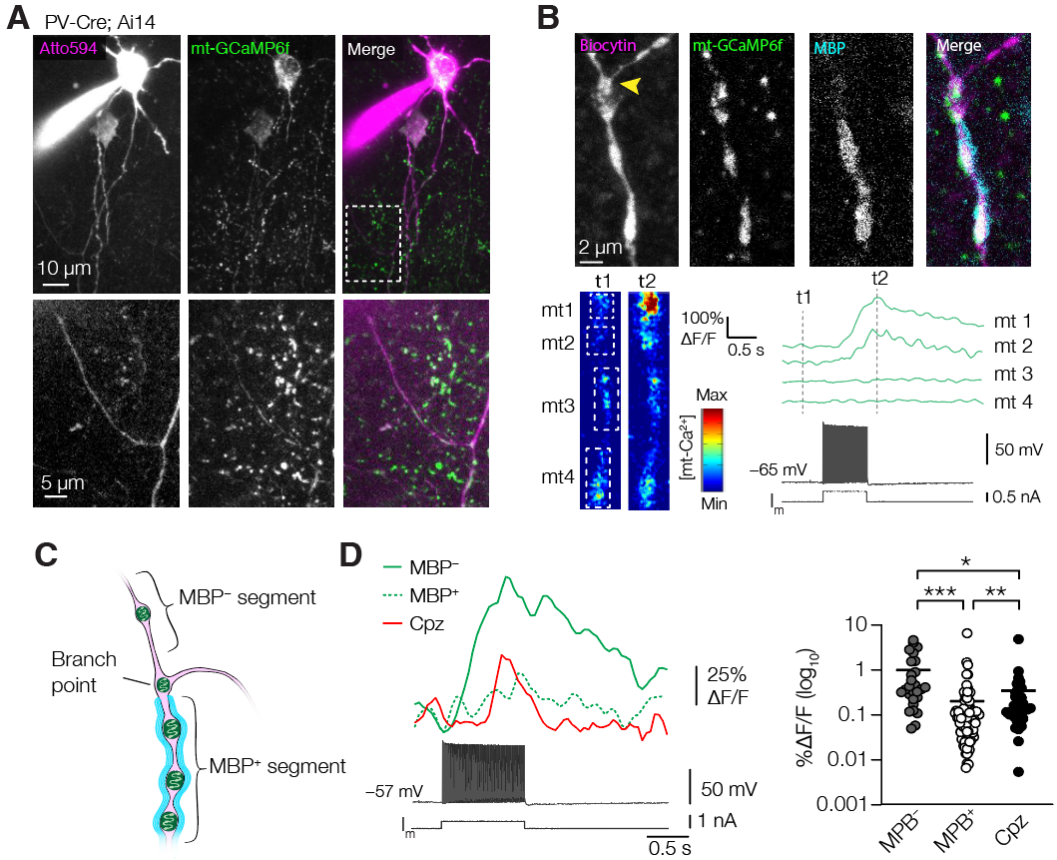


**Figure 6. Myelin attenuates mt-$Ca^{2+}$ responses. A** Example two-photon image of an Atto594-filled 4mtGcaMP6f$^+$ PV$^+$ interneuron. Dashed box indicates the first branch point of the axon, with a characteristic large angle (≥90°); **B** Example control PV$^+$ axon with mt-GCaMP6f-labeled mitochondria. Mt-$Ca^{2+}$ responses are much stronger in MBP$^-$ mitochondria (Mito 1 and 2) compared to those in MBP$^+$ segment (Mito 3 and 4). Dashed lines indicate timepoints corresponding to the heatmap, yellow arrowhead indicates branch point. **C** Schematic overview of sampled axonal regions. In d, for cuprizone, axonal segments in between branch points were selected. **D** *Left*, example $Ca^{2+}$ responses of mitochondria in MBP$^+$, MBP$^-$ or putatively demyelinated segments. *Right*, stronger mitochondrial $Ca^{2+}$ responses in MBP$^-$ segments compared to MBP$^+$ axon and increased $Ca^{2+}$ responses after demyelination (Kruskal-Wallis test, $P < 0.0001$; Dunn's post hoc test MBP$^-$ vs., MBP$^+$ ***$P < 0.0001$; MBP$^-$ vs. cuprizone, *$P = 0.0195$; MBP$^+$ vs. cuprizone, **$P = 0.0039$; MBP$^+$, $n = 101$ mitochondria of 12 cells from 7 mice; MBP$^-$, $n = 27$ mitochondria of 10 cells from 6 mice; cuprizone, $n = 36$ mitochondria of 10 cells from 5 mice). Solid bars in d represent the mean, individual data points represent mitochondria.

*Myelin loss impairs mitochondrial $Ca^{2+}$ responses at branch points*

Upon closer inspection of the localization of the mitochondria with large mt-$Ca^{2+}$ responses we found that they were located in close proximity to the outer edge of the myelin sheath or at branch points (**Figure 6B, 7A**). To obtain independent evidence for the precise localization of the myelin borders we immunostained for Caspr, revealing paranodes with an average length of 2.82 ± 0.18 µm (**Figure 7B**; $n = 36$ Caspr$^+$ segments of 3 cells from 2 mice). The Caspr$^+$ segments often flanked branch points if their branches were myelinated ($n = 19$ branch points of 4 cells from 3 mice, **Figure 7B**). In line with our initial observation, mitochondria were located closely next to the Caspr$^+$

10 signals (range 0.01–16.57 μm, average 2.46 ± 0.96 μm, $n$ = 20 paranodes of 4 cells from 3 mice,
11 **Figure 7C**). Interestingly, the mt-$Ca^{2+}$ buffering at branch points was indistinguishable in
12 amplitude in comparison to $MBP^{-}$ segments (**Supplementary Figure 4D**). These data suggest that
13 in $PV^{+}$ axons branch points are sites of nodes of Ranvier and mitochondria are clustered to the nodal
14 domains.

15 Finally, demyelination is associated with a loss of nodes of Ranvier (Dupree et al., 2004;
16 Crawford et al., 2009; Hamada and Kole, 2015). To understand whether the nodal mt-$Ca^{2+}$ buffering
17 was affected by myelin loss we therefore compared the branch point mt-$Ca^{2+}$ transients in control
18 and cuprizone-treated mice. The results showed that the AP-evoked mt-$Ca^{2+}$ transients in branch
19 points of demyelinated $PV^{+}$ axons were lower in amplitude (Mann-Whitney test, $P$ = 0.0123;
20 **Figure 7D**). Moreover, in putatively demyelinated $PV^{+}$ axons, mt-$Ca^{2+}$ responses in branch points
21 were indistinguishable from those in axonal segments (Mann-Whitney test, $P$ = 0.8106, **Figure**
22 **7E**). Together, these results suggest that the spatiotemporal distribution of mt-$Ca^{2+}$ buffering, with
23 hot spots clustered to branch points and low mt-$Ca^{2+}$ within the internodes, is disrupted by
24 demyelination (**Figure 8**).
25

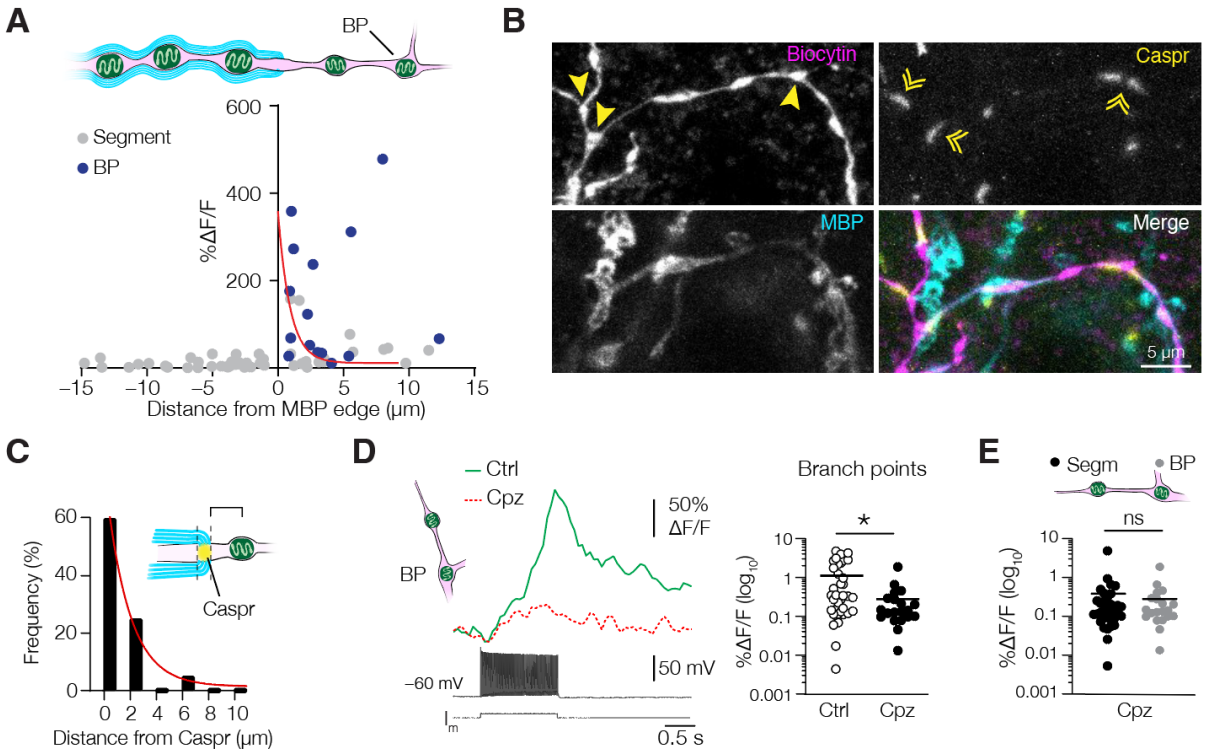


**Figure 7 – Demyelination reduces mt-$Ca^{2+}$ responses in $PV^+$ axonal branch points. A** Relation between distances from myelin sheaths and mt-$Ca^{2+}$ response amplitude. Red line indicates exponential decay fit (y = (3.588 – 0.1117) × exp(−0.894 × x) + 0.1117); *n* = 62 mitochondria of 9 cells from 6 mice). **B** Example confocal images of $PV^+$ axon branch points flanked by paranodes (Caspr). **C** Mitochondria are frequently found close to paranodes. Red line indicates exponential decay fit (y = (60.73 – 1.415) × exp(−0.5692 × x) + 1.415); *n* = 20 mitochondria of 4 cells from 3 mice. **D** *Left*, schematic representation of the compartments investigated in d and e; *Middle*, example traces from control or cuprizone-treated axon branch point mitochondria. *Right*, Amplitude of branch point mt-$Ca^{2+}$ responses was reduced upon demyelination (Mann-Whitney test, **P* = 0.0123; control, *n* = 38 mitochondria of 11 cells from 7 mice; cuprizone, *n* = 20 mitochondria of 9 cells from 5 mice). **E** In demyelinated $PV^+$ axons, mt-$Ca^{2+}$ responses at branch points are indistinguishable from those in segments (Mann-Whitney test, *P* = 0.8106; segment, *n* = 36 mitochondria of 10 cells from 5 mice, same data as Figure 6d; branch points, *n* = 20 mitochondria of 9 cells from 5 mice, same data as in d). BP, branch point. Solid bars in d and e represent the mean, individual data points represent mitochondria.

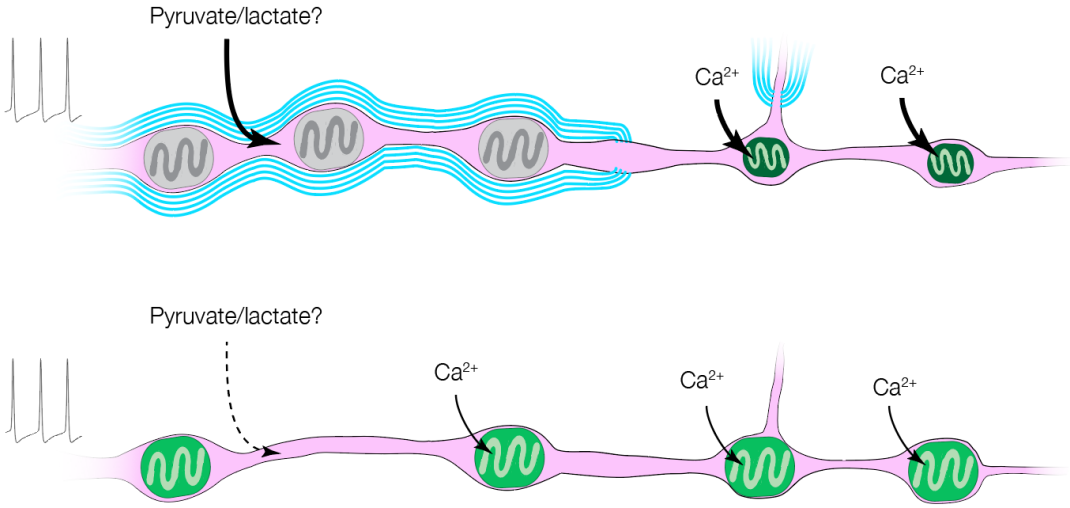


**Figure 8 – Summary of the effects of myelin loss on mitochondria in PV$^+$ axons**. In control PV$^+$ axons (top), mitochondria are clustered under the myelin sheath (cyan), possibly due to local delivery of nutrients such as pyruvate or lactate (arrow). Mitochondria at myelinated internodes are relatively large and display no or very weak activity-dependent mt-Ca$^{2+}$ transients (grey). In branch points and unmyelinated segments, AP-evoked mt-Ca$^{2+}$ transients are large (dark green). Following myelin loss (bottom), the mitochondrial pool becomes sparser, uniform and larger. The mt-Ca$^{2+}$ responses are uniform and low in amplitude (light green).

## Discussion

We used a Cre-dependent viral approach combined with single-cell reconstructions and found that myelinated segments of PV$^+$ axons are characterized by a higher mitochondrial content (**Figure 4, 5**). In addition, we found a myelin-dependent functional differentiation of the axonal mitochondrial pool; while mitochondria at branch points and unmyelinated segments in normally myelinated axons show strong mt-Ca$^{2+}$ buffering this pattern was disrupted after myelin loss, causing a uniform low mt-Ca$^{2+}$ uptake in demyelinated axons. Together, the results indicate that myelination branch-specifically shapes the mitochondrial pool in PV$^+$ axons.

The increased number of mitochondria we observed in myelinated PV$^+$ segments is in striking contrast with the general notion that myelinated axons have a low mitochondria content. Saturated ultrastructural reconstructions of the mouse neocortex show a ~30-fold decreased mitochondrial content in myelinated axons compared to unmyelinated axons (Kasthuri et al., 2015). Furthermore, demyelinated axons in the white matter region have an increased mitochondrial content in experimental demyelination models and multiple sclerosis (Kiryu-Seo et al., 2010; Nikic et al., 2011; Zambonin et al., 2011; Ohno et al., 2014; Licht-Mayer et al., 2020). Which factors underlie this distinct impact of myelin loss for PV$^+$ interneuron axons and regulate the clustering of

76 mitochondria to the internodes is unknown but likely involves both direct and indirect mechanisms.
77 Although internode membranes are typically considered to be passive and insulated by the myelin
78 sheath, recent experimental and computational work shows that during AP propagation the
79 internodal membrane, being partially electrically separated from the myelin sheath, produces
80 depolarizing waves with increasingly larger peak amplitudes near the edges of the sheath (Cohen
81 et al., 2020). Such depolarizations require ATP to activate the sodium potassium ATPase ($Na^+/K^+$
82 ATPase) pump to restore ionic gradients. Indeed, the internodal axolemma expresses high densities
83 of $Na^+/K^+$ ATPase (Young et al., 2008). Furthermore, live imaging in zebrafish axons showed that
84 near paranodes there is myelin-dependent vesicle release (Mensch et al., 2015; Almeida et al.,
85 2021), a process which requires high levels of ATP (Rangaraju et al., 2014). ATP consumption by
86 ATPases, vesicle release or other processes might cause high local cytoplasmic adenosine
87 diphosphate (ADP) levels, which are known to reduce mitochondrial motility (Mironov, 2007) and
88 thereby may potentially cluster mitochondria to $PV^+$ internodes. A hallmark of $PV^+$ interneuron
89 axons in the neocortex is their small diameter of on average ~0.3 µm for unmyelinated and ~0.6
90 µm for myelinated segments (Stedehouder et al., 2019; Micheva et al., 2021). Small diameter axons
91 possess a relatively large membrane surface/cytoplasm ratio which is less favourable for axial
92 conductivity and action potential propagation but also impedes transport and metabolic supply. The
93 energetic demand in these small diameter axons is further augmented by the high firing rates of
94 $PV^+$ interneurons and their generation of gamma frequencies (Kann et al., 2014). Based on the
95 increased mitochondrial clustering our data show that neocortical $PV^+$ interneuron axons heavily
96 rely on an external source of metabolic supply. The myelin sheath and axons of GABAergic neurons
97 also show multiple distinctive features in their molecular and cellular organization, including
98 different mitochondrial proteins (reviewed in Mazuir et al., 2021). The hypothesis of an external
99 supply requirement is in part supported by molecular analysis of the myelin sheath of GABAergic
00 axons showing higher levels of 2',3'-cyclic nucleotide 3'-phosphohydrolase (CNPase; Micheva et
01 al., 2018). CNPase is part of the cytoplasmic channels in myelin and oligodendrocytes involved in
02 lactate and pyruvate supply to the periaxonal space, where they are taken up by the axon via
03 monocarboxylate transporters (MCTs; Fünfschilling et al., 2012; Lee et al., 2012; Micheva et al.,
04 2018; Philips et al., 2021). Whether oligodendroglial lactate acts as a trophic factor to immobilize
05 axonal mitochondria remains to be tested. Interestingly, high glucose availability has been shown
06 to negatively regulate mitochondrial motility (Pekkurnaz et al., 2014). A limitation of the present
07 study is that we did not investigate mitochondrial motility within the proximal myelinated, branches
08 of demyelinated $PV^+$ axons (Ohno et al., 2011). Longitudinal imaging of $PV^+$ internodes could
09 provide critical insights into the temporal relationship between mitochondria and the myelin sheath.

While the molecular mechanisms and dynamics of $PV^+$ internode mitochondrial clustering remain to be further examined the present data indicate that the localization of mitochondria in $PV^+$ axons is strongly linked to myelination.

To determine the features of motility, $Ca^{2+}$ buffering, anatomical properties of size and shape as well as the distribution of the mitochondria in $PV^+$ interneurons we used two-photon and confocal microscopy, which have been used previously to study mitochondria (Mahad et al., 2009; Zambonin et al., 2011; Lewis et al., 2018; Kontou et al., 2021). Compared to other techniques such as EM(Witte et al., 2009) or stochastic optical reconstruction microscopy (STORM; Cserép et al., 2018), confocal imaging has the critical advantage of allowing the mapping of mitochondria in large parts of single cells which is especially useful in $PV^+$ interneurons, which are characterized by extensive three-dimensional axonal arborizations (**Figure 3**). Confocal and two-photon microscopy permit subcellular investigation of mitochondria, but we cannot exclude the possibility that small mitochondria exist that we were not able to detect, or that in some cases mitochondria were situated very close together and could not be separately identified, leading to an underestimation of the total mitochondria number. These limitations notwithstanding, our finding that dendritic mitochondria were larger and more tubular than their axonal counterparts are in good agreement with previous findings (Lewis et al., 2018). Moreover, that mitochondria in the $PV^+$ interneuron axon were significantly increased in size by ~60% upon demyelination (**Figure 3**, **Figure 4**) is in keeping with previous studies in axons of other cell types, indicating that our approach enabled us to identify canonical mitochondrial features associated with myelin loss (Witte et al., 2009; Nikic et al., 2011; Zambonin et al., 2011).

The diverse mt-$Ca^{2+}$ responses in $PV^+$ axons are likely to reflect local differentiation of the axon membrane or mitochondria specialisations. In normally myelinated axons we observed strong mt-$Ca^{2+}$ influx near branch points which were flanked by $Caspr^+$ signals. The presence of these axoglial junction glycoproteins suggest they are sites of nodes of Ranvier, consistent with previous work in GABAergic axons (Benamer et al., 2020; Mazuir et al., 2021). At the nodes APs are regenerated causing large local cytoplasmic $Ca^{2+}$ responses as recorded in other neuron types (Grundemann and Clark, 2015; Zhang and David, 2016; Hanemaaijer et al., 2020). The lower mt-$Ca^{2+}$ transients at these sites after demyelination might therefore reflect loss of nodal ion channel proteins and/or frequency-dependent failures during our trains of ~100 spikes. To distinguish between these possibilities patch-clamp recordings will need to be made at from demyelinated $PV^+$ axons to achieve a temporal resolution of single APs. The large mt-$Ca^{2+}$ transients at unmyelinated segments in control axons are, however, not well understood. These mitochondria may be located

near presynaptic GABAergic terminals where voltage-gated $Ca^{2+}$ channels drive major cytoplasmic $Ca^{2+}$ influx (Lewis et al., 2018; Ashrafi et al., 2020). However, mt-$Ca^{2+}$ transients near boutons typically show very large amplitudes (**Supplementary Figure 4**). A more likely possibility is that these mitochondria are close to small branch points which we were unable to resolve with confocal microscopy. Indeed, $PV^+$ axons have previously been described to possess very fine axonal branches that may be too small to detect with confocal imaging and instead require higher resolution obtained with array tomography (Micheva et al., 2021). Our finding that mitochondria in myelinated internodes of the $PV^+$ axon showed little, if any, $Ca^{2+}$ responses could be caused by differences in mitochondrial membrane potential or expression of proteins that gate mt-$Ca^{2+}$ such as the mitochondrial calcium uniporter (MCU) or its regulators (Giorgi et al., 2018). However, this functional differentiation is also in keeping with findings that the internodal axolemma shows lower amplitude depolarizations during AP propagation (Cohen et al., 2020), which might also explain the increased internodal mt-$Ca^{2+}$ transients we observed in demyelinated $PV^+$ segments.

The present finding that myelin clusters mitochondria and diversifies mitochondrial $Ca^{2+}$ buffering (which also drives ATP synthesis; Rizzuto et al., 2012) indicates that myelination at the level of branch orders may provide an axoglial mechanism to regulate energy homeostasis in $PV^+$ axons. An important caveat is that with our acute slice preparation the myelination state of the axonal segments prior to demyelination is unknown. Future studies could address this point using longitudinal *in vivo* imaging. It will also be important to study the cytosolic $Ca^{2+}$ levels in $PV^+$ axons at rest and during AP trains, as demyelination has been proposed to increase cytosolic $Ca^{2+}$ levels (Campbell and Mahad, 2012). The AAV approach introduced in the present study will be useful to deliver vectors that enable monitoring cytosolic ATP in a cell type-specific manner (Trevisiol et al., 2017) which will allow the study of axonal ATP levels in demyelinated $PV^+$ interneurons. Finally, our results also have implications for interneuron myelin plasticity (Stedehouder et al., 2018; Yang et al., 2020). Both myelination and proper mitochondrial distribution in $PV^+$ interneurons are known to be important for gamma oscillations, indicating converging pathways that underly $PV^+$ interneuron function (Kontou et al., 2021; Dubey et al., 2022). If in $PV^+$ interneurons newly formed myelin sheaths attract mitochondria this could represent a novel axoglial mechanism to selectively alter specific axonal pathways in the $PV^+$ interneuron, subsequently strengthening fast inhibitory transmission of specific neocortical connections. Future research will be necessary to test this hypothesis, by for instance using longitudinal mitochondrial imaging during development of myelination or activity-induced myelination.

78 **Supplemental Figures**
79

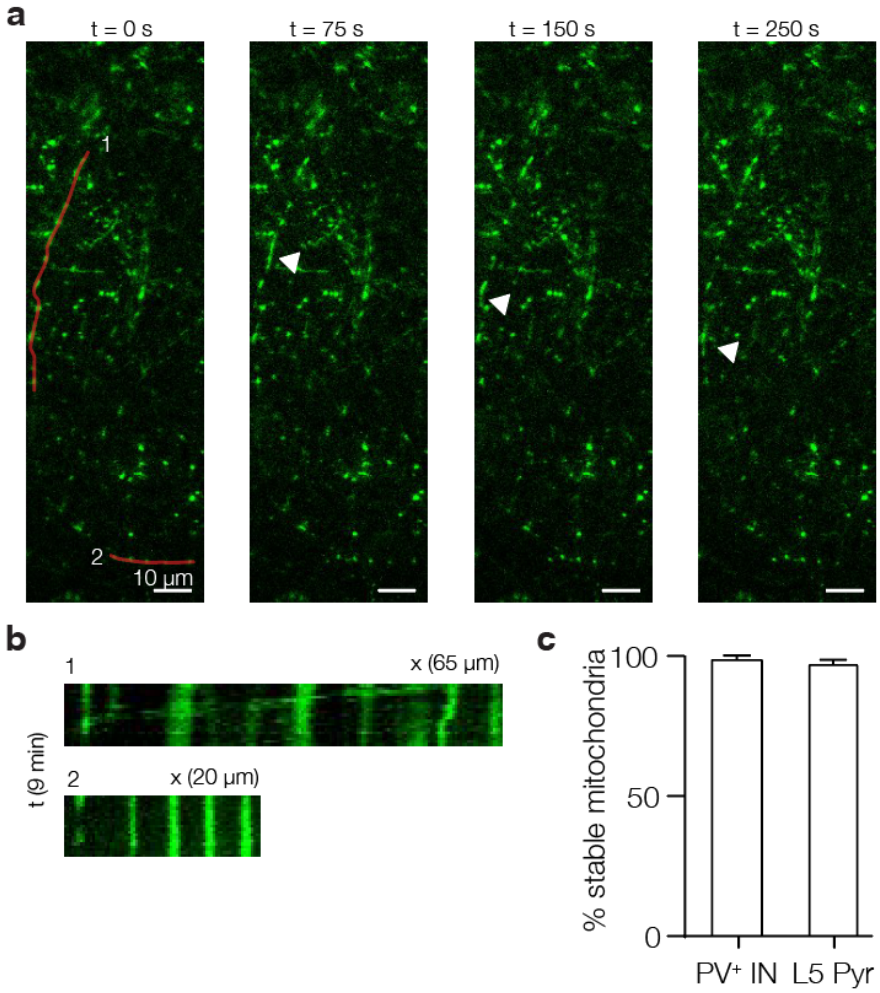


80
81
82 **Supplementary Figure 1 - Mitochondrial motility in acute brain slices A** Example frames
83 showing motile mitochondria (mt-GFP, green) in one L5 PN axon, but all other mitochondria are
84 stationary. Red lines indicate paths used for kymographs in (B). **B** Example kymographs showing
85 mitochondrial motility (1) and stability (2). **C** Quantification of stationary mitochondria in $PV^+$
86 interneurons (PV-Cre; Ai14 mice, $n$ = 4) or L5 pyramidal cells (Rbp4-Cre mice, $n$ = 3). PV-Cre;
87 Ai14, $n$ = 11/1236; Rbp4-Cre, $n$ = 23/1145 motile mitochondria/total mitochondria.
88

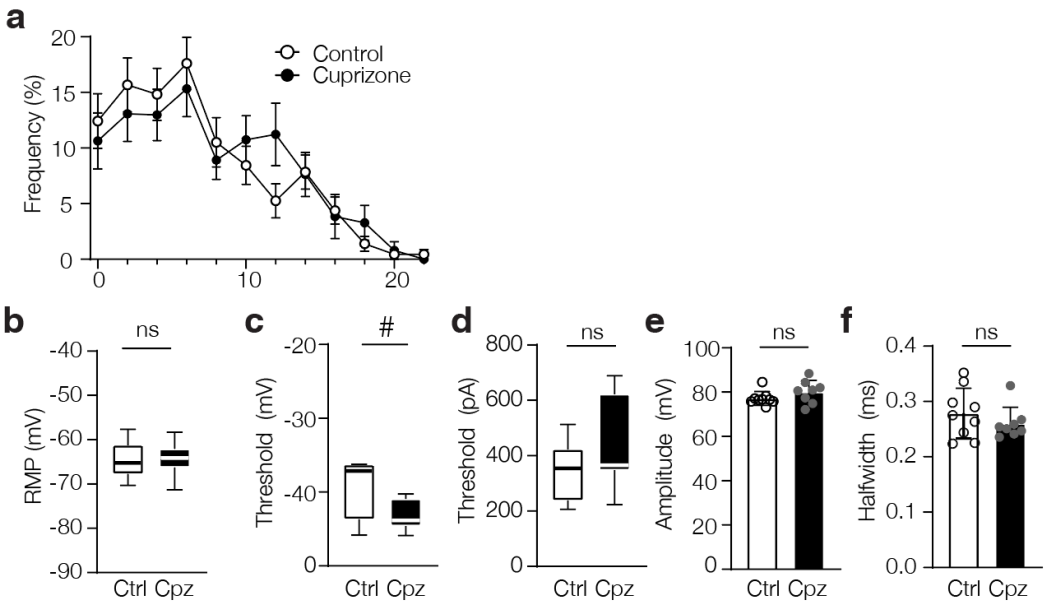


**Supplementary Figure 2 – Action potential parameters and mitochondrial distribution at the AIS upon demyelination. A** Mitochondria are unevenly distributed along the AIS length (two-way ANOVA, Distance from AIS origin $P < 0.0001$, $F_{(6.917, 304.3)} = 25.35$; control, $n = 215$ mitochondria in 27 AISs from 4 mice; cuprizone, $n = 144$ mitochondria in 18 AISs from 3 mice); Distribution is unaffected by cuprizone treatment (interaction effect $P = 0.7841$, $F_{(17,748)} = 0.7199$; treatment effect $p > 0.9999$, $F_{(1, 44)} = 0.000$, two-way ANOVA). **B** No change in resting membrane potential (RMP; unpaired t-test, $P = 0.7249$; control, $n = 9$ cells from 5 mice; cuprizone, $n = 8$ cells from 5 mice). **C** Voltage threshold shows a trend towards reduction upon cuprizone-mediated demyelination (unpaired t-test, $P = 0.0590$; control, $n = 9$ cells from 5 mice; cuprizone, $n = 8$ cells from 5 mice); No difference between control and cuprizone-treated groups in **D** current threshold (unpaired t-test, $P = 0.2066$), **E** AP amplitude (unpaired t-test, 0.1697) or **F** halfwidth (unpaired t-test, $P = 0.3489$; control, $n = 9$ cells from 5 mice; cuprizone, $n = 8$ cells from 5 mice). Bar graphs indicate the mean, individual data points represent cells, error bars indicate SEM; Box plots represent the 25$^{th}$ to 75$^{th}$ percentiles, whiskers indicate the maximal and minimal values, solid line represents the median.

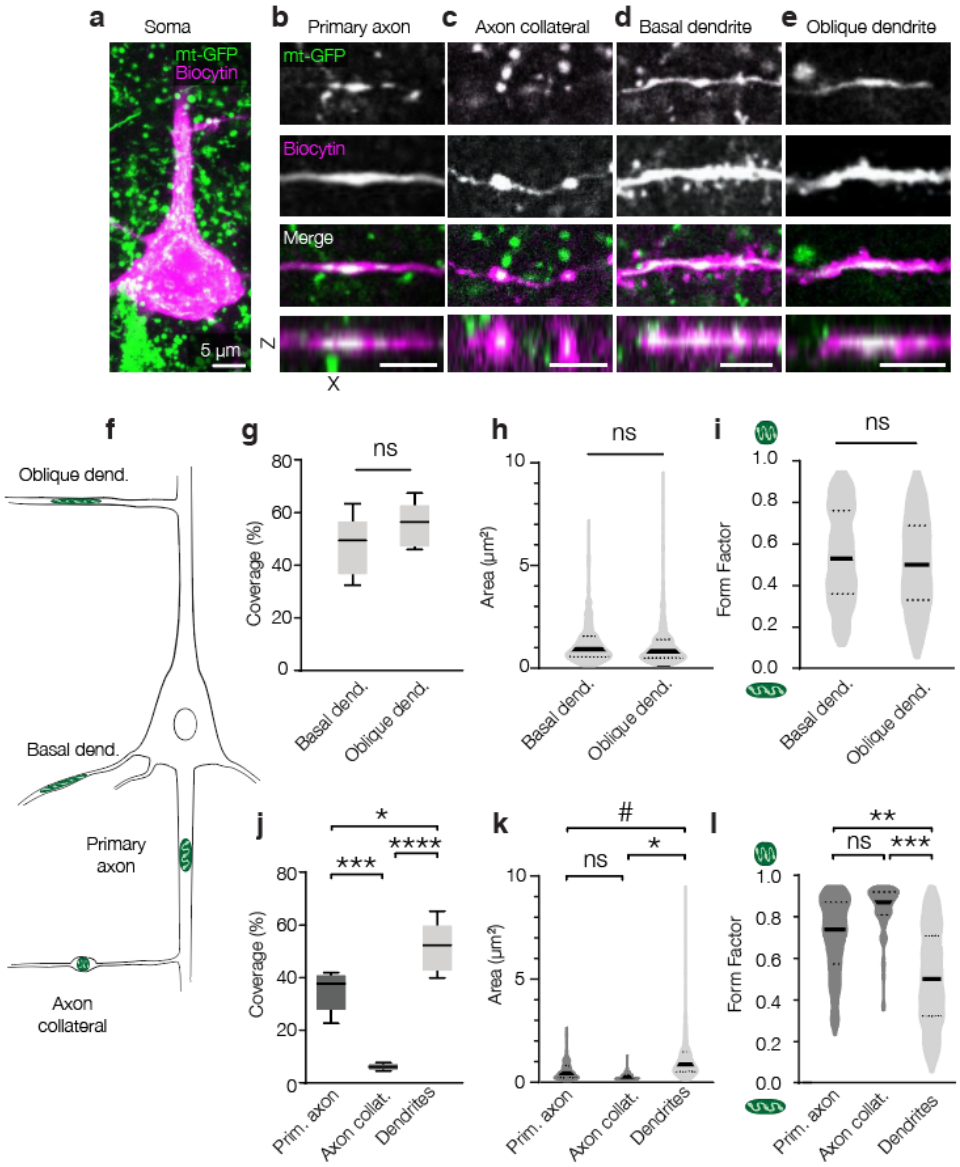


**Supplementary Figure 3 – Axonal mitochondria are distinct from those in dendrites in L5 PNs.** Example images of mitoGFP-labeled mitochondria in the **A** soma, **B** primary axon, **C** axon collateral, **D** oblique dendrite branch or **E** basal dendrite of a L5 pyramidal neuron. Somatic mitochondria were not quantified. **F** Schematic of subcellular compartments of the L5 PN that were investigated. **G** Dendritic coverage is not different between basal and oblique dendrites (unpaired t-test, $P = 0.2538$; basal dendrites, $n = 321$; oblique dendrites, $n = 331$ mitochondria from 5 cells of 3 mice each for each). **H** Mitochondria from basal and oblique dendrites have similar surface area (nested t-test, $P = 0.9554$) and **I** form factor (nested t-test, $P = 0.6994$; basal dendrites, $n = 321$; oblique dendrites, $n = 331$ mitochondria from 5 cells of 3 mice each for each). Basal dendrites, $n = 321$; oblique dendrites, $n = 331$ mitochondria from 5 cells of 3 mice each. **J** Neurite length covered by mitochondrial length (one-way ANOVA, $P < 0.0001$; Bonferroni's post hoc test, Primary axon vs axon collaterals, ***$P = 0.0001$; primary axon vs dendrites, **$P = 0.0141$; axon collateral vs dendrites, ****$P < 0.0001$; primary axon $n = 188$, axon collateral $n = 125$, dendrites $n = 652$ mitochondria; for each, $n = 5$ cells from 3 mice). **K** Mitochondrial area in L5 PNs is largest

in dendrites and smallest in axon collaterals (nested one-way ANOVA, *$P$ = 0.0192; Bonferroni's post hoc test, primary axon vs axon collaterals $P > 0.9999$; primary axon vs dendrites, #$P$ = 0.0917; axon collaterals vs dendrites, *$P$ = 0.0241; primary axon $n$ = 188, axon collateral $n$ = 125, dendrites $n$ = 652 mitochondria; for each, $n$ = 5 cells from 3 mice). **L** Mitochondria are significantly more round in L5 PN axons compared to dendrites. A value of 1 reflects a perfect circle, which flattens out as values move closer to 0 (nested one-way ANOVA, $P$ = 0.0003; Bonferroni's post hoc test, primary axon vs axon collaterals, $P$ = 0.2132; primary axon vs dendrites, **$P$ = 0.0068; axon collaterals vs dendrites, ***$P$ = 0.0003; primary axon $n$ = 188, axon collateral $n$ = 125, dendrites $n$ = 652 mitochondria; for each, $n$ = 5 cells from 3 mice). Box plots represent the 25$^{th}$ to 75$^{th}$ percentiles, whiskers represent the maximal and minimal values, solid line represents the median. In truncated violin plots, solid lines represent the median, dotted lines represent 25$^{th}$ and 75$^{th}$ quartiles.

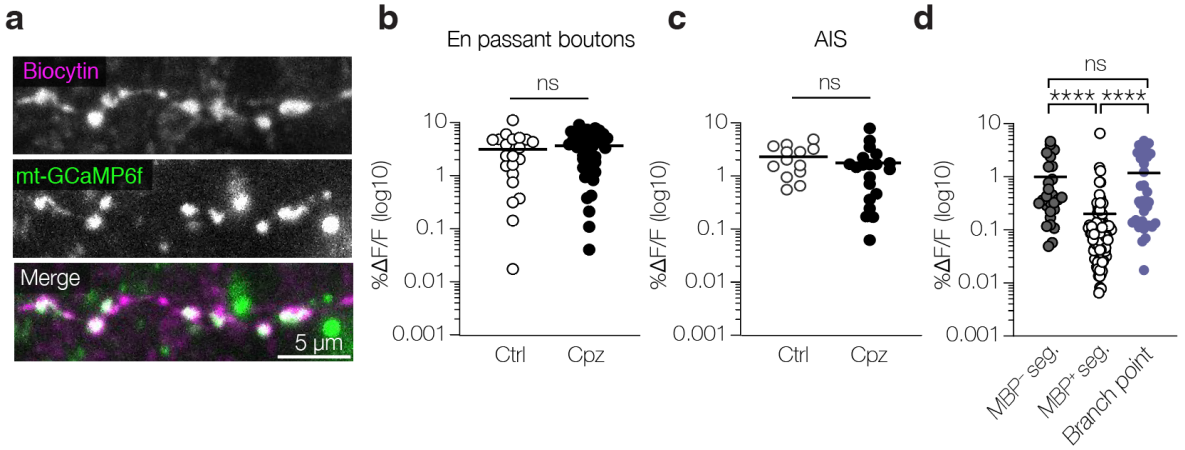


**Supplementary Figure 4 – A** Example confocal image of PV$^+$ *en passant* boutons. **B** Demyelination does not alter mt-Ca$^{2+}$ buffering in *en passant* boutons (Mann-Whitney test, $P$ = 0.2847; control, $n$ = 21 mitochondria of 4 cells from 2 mice; cuprizone, $n$ = 47 mitochondria of 8 cells from 4 mice). **C** mt-Ca$^{2+}$ responses at the AIS are not changed after demyelination (Mann-Whitney test, $P$ = 0.1694; control, $n$ = 15 mitochondria of 5 AISs from 3 mice; cuprizone, $n$ = 20 mitochondria of 6 AISs from 4 mice). **D** In control PV$^+$ axons, amplitude of mt-Ca$^{2+}$ responses at MBP$^-$ segments are not different from those at branch points (Kruskal-Wallis test, $P$ < 0.0001; Dunn's post hoc test, MBP$^+$ vs MBP$^-$ $P$ = 0.0020, MBP$^-$ vs. branch points $P$ > 0.9999; MBP$^+$ vs branch points $P$ < 0.0001; MBP$^+$ segments, $^+$, $n$ = 101 mitochondria of 12 cells from 7 mice, same data as in Figure 7d; MBP$^-$ segments, $n$ = 27 mitochondria of 9 cells from 5 mice, same data as in Figure 6d; branch points, $n$ = 38 mitochondria of 11 cells from 7 mice, same data as in Figure 7d; $n$ = 21 mitochondria of 4 cells from 2 mice, same data as in b). Responses in *en passant* boutons are larger compared to those in MBP$^-$ segments (Mann-Whitney test, $P$ = 0.0009). Individual data points represent mitochondria, solid bars represent means.

**Supplementary Table 1**

| Antibody | Host | Dilution | Manufacturer | Catalog number | RRID |
|---|---|---|---|---|---|
| Anti-Green fluorescent protein | Chicken | 1:500 | Abcam | ab13970 | AB_300798 |
| Anti-Red fluorescent protein | Mouse | 1:500 | Abcam | ab65856 (discontinued) | AB_1141717 |
| Anti-βIV Spectrin | Rabbit | 1:1000 | Engelhardt and Kole lab | N/A | N/A |
| Anti-Myelin Basic Protein | Mouse | 1:250 | Covance | SMI-99P | AB_10120129 |
| Anti-Mouse-Alexa-405 | Goat | 1:500 | ThermoFisher | A31553 | AB_221604 |
| Anti-Chicken-Alexa-488 | Goat | 1:500 | ThermoFisher | A11039 | AB_142924 |
| Anti-Rabbit-Alexa-633 | Goat | 1:500 | ThermoFisher | A21070 | AB_2535731 |
| Anti-Mouse-Alexa-647 | Goat | 1:500 | ThermoFisher | A21235 | AB_2535804 |
| Streptavidin-Alexa-594 | N/A | 1:500 | ThermoFisher | S11227 | N/A |
| Streptavidin-Alexa-633 | N/A | 1:500 | ThermoFisher | S32364 | AB_2313500 |

**Supplementary Table 1.** Overview of antibodies and dilutions used in this study.

70 **Methods**

71 *Animals*

72 All procedures were performed after evaluation by the Royal Netherlands Academy of Arts and
73 Sciences (KNAW) Animal Ethics Committee (DEC) and Central Authority for Scientific
74 Procedures on Animals (CCD, license AVD8010020172426). The specific experimental designs
75 were evaluated and monitored by the Animal Welfare Body (IvD, protocols NIN19.21.01,
76 NIN19.21.09 and NIN19.21.12). Male and female PV-Cre; Ai14, Rbp4-Cre or Rbp4-Cre; ChETA
77 mice were used in this study that were kept at a 12h day-night cycle with access to food *ad libitum*.
78 At 8 weeks of age, mice were fed either food with or without 0.2% cuprizone (biscyclohexane
79 oxaldihydrazone, Sigma-Aldrich) supplement (range: 5-6 weeks). During this time, the weight and
80 overall welfare of the mice was closely monitored.

81

82 *Plasmids*

83 Cre-dependent mt-GFP and mt-GCaMP6f AAV plasmids was created by replacing the mCherry
84 open reading frame (ORF) in pAAV-EF1a-mCherry-DIO (Addgene plasmid #20299, RRID:
85 Addgene_20299) with mt-GFP or 4mt-GCaMP6f ('mt-GcAMP6f' in the main text). High-Fidelity
86 Phusion Taq polymerase (Thermo Fisher Scientific, F-530XL) was used to amplify mt-GFP from
87 Addgene plasmid #44385 (RRID: Addgene_44385) or 4mt-GCaMP6f (plasmid was generously
88 donated by Diego de Stefani). For mt-GFP, PCR fragment and plasmid were digested with AscI
89 and NheI (New England Biolabs). Because 4mt-GCaMP6f contains an NheI digestion site, to create
90 the mt-GCaMP6f-DIO plasmid, pAAV-EF1a-mCherry-DIO was digested with NheI, blunted using
91 T4 DNA Polymerase (New England Biolabs), digested with AscI and then dephosphorylated using
92 Antarctic Phosphatase (New England Biolabs). The 4mt-GCamP6f PCR product was
93 phosphorylated using T4 Polynucleotide Kinase (New England Biolabs) and digested using AscI.
94 Plasmid and insert were then ligated overnight at 16 °C (T4 DNA ligase, New England Biolabs).
95 After transformation into chemically competent *E.coli* and subsequent plasmid purification,
96 insertion and double inverted orientation (DIO) were confirmed using restriction enzyme analysis
97 and DNA sequencing. The plasmids were deposited to Addgene (mt-GFP-DIO #174112;
98 4mtGCaMP-DIO: #179529). To test Cre-dependent expression, HEK293-T cells (HEK 293T/17
99 cell line, CRL-11268 obtained from ATCC; RRID:CVCL_1926) were transfected with pAAV-
00 EF1a-mt-GFP-DIO or pAAV-EF1a-mt-GCaMP6f-DIO only or pAAV-EF1a-mt-GFP-DIO and
01 pCAG-Cre (Addgene #13775; RRID Addgene_13775) using polyethylenimine (PEI). Briefly,
02 plasmid DNA (500 ng) was diluted in saline and then mixed with PEI, allowed to incubate for 20-
03 25 minutes and then applied dropwise to HEK293-T cells in a 6-well plate. MitoGFP or mt-

GCaMP6f expression was assessed the next day using a fluorescence microscope, which was absent in the cells lacking or expressing only pCAG-Cre, confirming Cre-dependence.

mt-GFP primers :
FW: 5' – AATAGCTAGCATCATGTCCGTCCTGACG – 3'
RV: 5' - TAATGGCGCGCC GGAAGTCTGGACATTTATTTG – 3'
4mt-GCaMP6f primers:
FW: 5' – ACT TCG CTG TCA TCA TTT G– 3'
RV: 5' - GCTAGCCCACCATGTCCGTC– 3'
Sequencing primers:
FW: 5' – GGATTGTAGCTGCTATTAGC – 3'
RV: 5' – GGCAAATAACTTCGTATAGGA – 3'

*AAV production*

HEK293-T cells of low passage (<25) were kept in Dulbecco′s Modified Eagle′s Medium (DMEM, Thermo Fisher Scientific #31966-047) containing 10% fetal calf serum (FCS, Thermo Fisher Scientific A4766801) and 5% penicillin-streptomycin (Pen-Strep, Thermo Fisher Scientific #15140122) at 37 °C and 5% $CO_2$. For virus production, cells were plated on 15 cm dishes at a density of 1-1.25 × $10^7$ cells per dish (12 dishes per virus). The next day, medium was replaced with Iscove's Modified Dulbecco's Medium (IMDM, Sigma Aldrich I-3390) containing 10% FCS, 5% Pen-Strep and 5% glutamine (Thermo Fisher Scientific #25030081) 1-2 hours before transfection. For transfection, AAV rep/cap, AAV helper (mt-GFP: AAV5; mt-GCaMP6f: AAV1) and transfer plasmids were mixed and diluted in saline before mixing with saline-diluted polyethylenimine (PEI, Polysciences #23966-2) and brief vortexing. After 20-25 minutes of incubation, the transfection mix was added in a drop-wise fashion to the culture plates. The next day, all medium was refreshed after which the cells were left for an additional two nights (*i.e.* 72 hours after transfection). Medium was discarded and cells were then collected and subsequently lysed with 3 freeze-thaw cycles to release AAVs. Cell lysate was then loaded on an iodixanol gradient (60, 40, 25 and 15% iodixanol, ELITechGroup #1114542) in Beckman Quick-Seal Polyallomer tubes (Beckman-Coulter #342414) which were sealed and centrifuged in a Beckman-Coulter Optima XE-90 Ultracentrifuge at 16 °C and 69,000 rpm for 1 hour and 10 minutes. The virus-containing fraction was extracted from the tubes and AAVs were then concentrated in Dulbecco's Phosphate Buffered Saline (D-PBS) + 5% sucrose using Amicon Ultra-15 (100K) filter units (Merck Millipore UFC910024) at 3220 *g*. At least 4 rounds of centrifugation were used to

38 ensure complete replacement of iodixanol with D-PBS + 5% sucrose. Typical yields were ~150 µl
39 of virus, the titer of which was determined using quantitative PCR (titers: mt-GFP-DIO, 4.43 ×
40 $10^{13}$ gc/ml; mt-GCaMP6f-DIO, 3.44 × $10^{13}$ gc/ml) (Aurnhammer et al., 2012). Viral aliquots were
41 stored at −80 °C until further use.
42
43 qPCR primers, recognize AAV2 Inverted Terminal Repeats (ITRs):
44 5' – GGAACCCCTAGTGATGGAGTT – 3'
45 5' – CGGCCTCAGTGAGCGA – 3'
46
47 *Viral injection*
48 Viral injections were typically performed during the 3rd week of control powder food or cuprizone
49 treatment. Mice were anaesthetized using isoflurane (3% induction, 1.2–1.5% maintenance) after
50 which they subcutaneously received 5mg/kg Metacam. Body temperature was monitored and
51 maintained at 37 °C using a heating pad and eyes were prevented from drying out using eye
52 ointment to prevent. The head was then shaved and placed in a stereotaxic frame (Kopf) and an
53 incision was made in the skin along the midline. Lidocaine (10%) was administered on the periost
54 before removing it. Small (<1 mm) bilateral craniotomies were made at -0.5 mm caudally from
55 Bregma and 2.5 mm laterally from the midline without damaging the dura mater. With a sharp glass
56 pipet attached to a Nanoject III (Drummond), 40-50 nL of virus was injected at 1 nL/second and at
57 a depth of 450 µm. Approximately 3 minutes after finishing the injection, the needle was retracted
58 slowly. Bone wax was applied to the craniotomies and the skin was sutured before the animal was
59 allowed to recover.
60
61 *Acute slice preparation*
62 After 5-6 weeks of cuprizone or control treatment (*i.e.* 2-3 weeks after virus injection), mice were
63 deeply anaesthetized using pentobarbital (50 mg/kg, intraperitoneal injection) and transcranially
64 perfused with ice-cold carbogenated (95% $O_2$, 5% $CO_2$) cutting artificial cerebrospinal fluid
65 (cACSF; 125 mM NaCl, 3 mM KCl, 6 mM $MgCl_2$, 1 mM $CaCl_2$, 25 mM glucose, 1.25 mM
66 $NaH_2PO_4$, 1 mM kynurenic acid and 25 mM $NaHCO_3$). After quickly dissecting out the brain 400
67 µm thick parasagittal slices were cut in ice-cold carbogenated cACSF using a Vibratome (1200S,
68 Leica Microsystems). Slices were transferred to a holding chamber containing carbogenated cACSF
69 where they were kept at 35 °C for 35 min to recover and then allowed to return to room temperature
70 for at least 30 min before starting experiments.

*Electrophysiology and two-photon imaging*

To perform electrophysiological experiments, slices were transferred to a recording chamber with continuous in- and outflow of carbogenated recording ACSF (rACSF, 125 mM NaCl, 3 mM KCl, 1 mM $MgCl_2$, 2 mM $CaCl_2$, 10 mM glucose, 5 mM L-Lactate, 1.25 mM $NaH_2PO_4$, and 25 mM $NaHCO_3$) at a rate of 1-2 ml per minute at 32 °C. Glass pipettes with an open tip resistance of 6-7 MΩ were filled with an intracellular solution containing (in mM, 130 K-Gluconate, 10 KCl, 10 HEPES, 4 Mg-ATP, 0.3 $Na_2$-GTP, 10 $Na_2$-phosphocreatine; pH ~7.25, osmolality ~280 mOsmol/kg) supplemented with 5 mg/ml biocytin (Sigma-Aldrich, B4261) and 50 µM Atto-594 (Sigma-Aldrich, A08637). Whole-cell recordings were made using a patch-clamp amplifier (Multiclamp 700b, Axon Instruments, Molecular Devices, RRID: SCR_018455) operated by AxoGraph X software (version 1.5.4; RRID: SCR_014284). Action potential trains were evoked using 700 ms step pulses, from −250 pA to +700 nA with increments of 50 pA. Single action potentials were evoked using 3 ms incremental (2.5-5 pA) step pulses with a starting amplitude below spike threshold. Using an AD/DA converter (ITC-18, HEKA Elektronik GmbH), voltage was digitally sampled at 100 Hz. The access resistance during current-clamp experiments (range: 15–30 MΩ) was fully compensated using bridge balance and capacitance neutralization of the amplifier. Somatic single-cell recordings were made from mt-GFP$^+$ cells, which were visualized using a two-photon (2P) laser-scanning microscope (Femto3D-RC, Femtonics Inc., Budapest, Hungary). Imaging was controlled using MES software (Femtonics Inc., Budapest, Hungary, version 6.3.7902). A Ti:Sapphire pulsed laser (Chameleon Ultra II, Coherent Inc., Santa Clara, CA, USA) was tuned to 770 nm for two-photon excitation to visualize mt-GFP/mt-GCaMP6f and tdTomato. Fluorescent signals were detected using two photomultipliers (PMTs, Hamamatsu Photonics Co., Hamamatsu, Japan), one for mt-GFP and for Atto-594 (20 µM) to assess its diffusion, as an indication of biocytin diffusion. For motility imaging, *Z*-stacks were acquired every 10 s for 8-12 mins. The Image Stabilizer plugin for FIJI was used to account for drift. For $Ca^{2+}$ imaging, mt-GCaMP6f$^+$ cells were targeted for single-cell patch clamping and filled with Atto-594 (50 µM) and biocytin (5 mg/ml). Next, Z-stacks were made with the laser tuned to 800 nm to identify the axon using the Atto-594 signal. Mitochondrial $Ca^{2+}$ responses were then visualized with the laser tuned to 940 nm and recorded at ~20 Hz imaging frequency. $Ca^{2+}$ responses were analysed using a custom-written Matlab script. Briefly, regions of interest containing mitochondria were selected from which background was subtracted, bleach correction and smoothing were applied, and ΔF/F was calculated. Care was taken to keep the number of APs, which were evoked

using a 700 ms block pulse, the same between groups ($MBP^-$, 105.6 ± 0.89 action potentials; $MBP^+$, 103.6 ± 0.51 APs; cuprizone, 104.7 ± 1.06 APs, Kruskal-Wallis test $P = 0.1591$).

*Immunohistochemistry*

For staining of biocytin-filled cells, upon completion of experiments acute slices were immediately placed into 4% PFA in PBS for 20-25 minutes, followed by 3 washes of 10 minutes with PBS. Next, tissue was blocked for 2 hours in PBS containing 1-2% Triton-X and 10% normal goat serum. After blocking, sections were moved to blocking buffer containing primary antibodies (**Supplementary Table 1**) and were incubated overnight at room temperature. Following three 10 min washes in PBS, sections were transferred to PBS containing secondary antibodies (**Supplementary Table 1**) and were incubated overnight two hours room temperature or overnight at 4 °C. The tissue was finally washed again in PBS three times for 10 minutes before mounting using FluorSave mounting medium (Merck-Millipore #345789). For immunostainings against MBP, the staining protocol was adjusted: blocking was done one hour at 37 °C and one hour room temperature and using 1% Triton, tissue was washed only once in PBS per washing step, and secondary antibodies were incubated one hour at 37 °C and one hour room temperature. For immunostainings on sections without biocytin-filled cells, 400 µm PFA-fixed sections were first cryoprotected by placing them into 30% sucrose-PBS solution until fully saturated. A sliding freezing microtome (Zeiss Hyrax S30; temperature controlled by a Slee Medical GmbH MTR fast cooling unit) was used to cut 40 µm sections, which were either placed in PBS for immediate use or stored at −20 °C in cryoprotectant solution (30% ethylene glycol, 20% glycerol, 0.05 M phosphate buffer) until further use. Immunostaining protocol was the same as for 400 µm sections, but the blocking buffer contained 0.5% Triton-X and incubation duration for secondary antibodies was two hours at room temperature. All steps are performed with gentle shaking, with the exception of the 37 °C incubation steps.

*Confocal microscopy*

Imaging was performed using a Leica SP5 or SP8 X confocal laser scanning microscope controlled by Leica Application Suite AF. Biocytin-filled cells were imaged with a 63× oil-immersion lens using the tile-scan function with automated sequential acquisition of multiple channels enabled. Step sizes in the Z-axis were 0.3-0.75 µm, and images were collected at a 2048 × 2048 pixel resolution at 100-150 Hz. Mitochondria at AISs were imaged similarly, but only cells were imaged whose AIS was directed parallel to the imaging plane, and *Z*-stack step sizes were 0.2 µm. Cellular reconstructions and quantification of mitochondrial density and morphology in single cells or at the

AIS were performed manually using Neurolucida Software (MBF Bioscience, version 2020.1.3, 64 bit, RRID: SCR_001775). In $PV^+$ interneurons, axons could easily be distinguished from dendrites based on their small diameter and extensive branching. Mitochondrial contours were drawn at the plane where the mt-GFP signal was brightest and was omitted when neurite branches deviated strongly from a parallel orientation with respect to the imaging plane (their location was still marked for density calculations). Mitochondria were counted as belonging to the reconstructed cell if the mt-GFP signal was located clearly inside the cytosol and followed the path of the reconstructed neurite. After completion of tracing, reconstructions and contours were analysed using Neurolucida Explorer (MBF Bioscience, 2019.2.1, RRID: SCR_017348), which calculated contour area, form factor, density, axonal length and inter-mitochondrial distance. For analysis of mitochondrial densities at the myelin sheath, the MBP signal was turned off during tracing of $PV^+$ axons and marking their mitochondria, and *vice versa*. FIJI (RRID: SCR_002285) was used to extract partial images for use in figures. After preprocessing in FIJI, Imaris software (Oxford Instruments, version 9.7.2, RRID: SCR_007370) was used to generate three-dimensional surface renderings. The spot functionality of Imaris was used to count mitochondria in the field of view for motility analysis. Motile mitochondria were identified by eye, mitochondria were considered stable if they displaced less than 2 µm.

*Statistical analyses*

All statistical comparisons were done using Prism (Graphpad, version 8.4.3, RRID: SCR_002798). Normality of datasets was determined using D'Agostino & Pearson or Shapiro-Wilk tests. We applied non-parametric tests if data deviated significantly from a normal distribution. For comparisons between groups we used a two-tailed unpaired t-test (normal data) or a two-tailed Mann-Whitney test (non-normal data). For t-tests degrees of freedom (df) are reported in the figure legends. One-way ANOVA (normal data) or Kruskal-Wallis test (non-normal data) was applied for comparisons of three groups; two-way ANOVA was used to test interactions between groups and treatments; Bonferroni's post hoc test (normal data) or Dunn's post hoc test (non-normal data) was used for multiple comparisons; nested t-tests or nested one-way ANOVAs were used when large numbers of datasets were involved (*i.e.* mitochondrial contours) to avoid overpowering of non-nested statistical tests (cells were nested inside their respective treatment groups). Figure legends contain *P*-values and *n*-numbers and whether the latter signify animals, cells or mitochondria. Means are presented with SEM.

*Data availability*

All data and code are available upon request to the authors.

## References


Almeida RG, Williamson JM, Madden ME, Early JJ, Voas MG, Talbot WS, Bianco IH, Lyons DA (2021) Myelination induces axonal hotspots of synaptic vesicle fusion that promote sheath growth. Curr Biol.

Ashrafi G, Juan-Sanz J de, Farrell RJ, Ryan TA (2020) Molecular Tuning of the Axonal Mitochondrial Ca2+ Uniporter Ensures Metabolic Flexibility of Neurotransmission. Neuron 105:678-687.e5.

Aurnhammer C, Haase M, Muether N, Hausl M, Rauschhuber C, Huber I, Nitschko H, Busch U, Sing A, Ehrhardt A, Baiker A (2012) Universal Real-Time PCR for the Detection and Quantification of Adeno-Associated Virus Serotype 2-Derived Inverted Terminal Repeat Sequences. Hum Gene Ther Part B Methods 23:18–28.

Benamer N, Vidal M, Balia M, Angulo MC (2020) Myelination of parvalbumin interneurons shapes the function of cortical sensory inhibitory circuits. Nat Commun 11:5151.

Campbell GR, Mahad DJ (2012) Mitochondrial changes associated with demyelination: Consequences for axonal integrity. Mitochondrion 12:173–179.

Cohen CCH, Popovic MA, Klooster J, Weil MT, Mobius W, Nave KA, Kole MHP (2020) Saltatory Conduction along Myelinated Axons Involves a Periaxonal Nanocircuit. Cell 180:311--322.e15 Available at: https://pubmed.ncbi.nlm.nih.gov/31883793/.

Crawford DK, Mangiardi M, Xia X, López-Valdés HE, Tiwari-Woodruff SK (2009) Functional recovery of callosal axons following demyelination: a critical window. Neuroscience 164:1407–1421.

Cserep C, Posfai B, Schwarcz AD, Denes A (2018) Mitochondrial ultrastructure is coupled to synaptic performance at axonal release sites. Eneuro 5.

Cserép C, Pósfai B, Schwarcz AD, Dénes Á (2018) Mitochondrial Ultrastructure Is Coupled to Synaptic Performance at Axonal Release Sites. Eneuro 5:ENEURO.0390-17.2018.

Dubey M, Pascual-Garcia M, Helmes K, Wever DD, Hamada MS, Kushner SA, Kole MHP (2022) Myelination synchronizes cortical oscillations by consolidating parvalbumin-mediated phasic inhibition. Elife 11.

Dupree JL, MASON JL, Marcus JR, Stull M, Levinson R, Matsushima GK, Popko B (2004) Oligodendrocytes assist in the maintenance of sodium channel clusters independent of the myelin sheath. Neuron Glia Biol 1:179–192.

Dutta R, McDonough J, Yin X, Peterson J, Chang A, Torres T, Gudz T, Macklin WB, Lewis DA, Fox RJ, Rudick R, Mirnics K, Trapp BD (2006) Mitochondrial dysfunction as a cause of axonal degeneration in multiple sclerosis patients. Ann Neurol 59:478--489.

Edgar JM, McLaughlin M, Werner HB, McCulloch MC, Barrie JA, Brown A, Faichney AB, Snaidero N, Nave K, Griffiths IR (2009) Early ultrastructural defects of axons and axon–glia junctions in mice lacking expression of Cnp1. Glia 57:1815–1824.

Evangelou N, Konz D, Esiri MM, Smith S, Palace J, Matthews PM (2001) Size-selective neuronal changes in the anterior optic pathways suggest a differential susceptibility to injury in multiple sclerosis. Brain 124:1813–1820.

Fecher C, Trovo L, Muller SA, Snaidero N, Wettmarshausen J, Heink S, Ortiz O, Wagner I, Kuhn R, Hartmann J, Karl RM, Konnerth A, Korn T, Wurst W, Merkler D, Lichtenthaler SF, Perocchi F, Misgeld T (2019) Cell-type-specific profiling of brain mitochondria reveals functional and molecular diversity. Nat Neurosci 22:1731--1742.

Fünfschilling U, Supplie LM, Mahad D, Boretius S, Saab AS, Edgar J, Brinkmann BG, Kassmann CM, Tzvetanova ID, Möbius W, Diaz F, Meijer D, Suter U, Hamprecht B, Sereda MW, Moraes CT, Frahm J, Goebbels S, Nave K-A (2012) Glycolytic oligodendrocytes maintain myelin and long-term axonal integrity. Nature 485:517–521.

Gerfen CR, Paletzki R, Heintz N (2013) GENSAT BAC Cre-Recombinase Driver Lines to Study the Functional Organization of Cerebral Cortical and Basal Ganglia Circuits. Neuron 80:1368–1383.

Giorgi C, Marchi S, Pinton P (2018) The machineries, regulation and cellular functions of mitochondrial calcium. Nat Rev Mol Cell Bio 19:713–730.

Grundemann J, Clark BA (2015) Calcium-Activated Potassium Channels at Nodes of Ranvier Secure Axonal Spike Propagation. Cell Reports 12:1715--1722.

Hamada MS, Goethals S, Vries SID, Brette R, Kole MHP (2016) Covariation of axon initial segment location and dendritic tree normalizes the somatic action potential. Proc National Acad Sci 113:14841--14846 Available at: https://www.pnas.org/content/113/51/14841 https://www.pnas.org/content/113/51/14841.abstract.

Hamada MS, Kole MHP (2015) Myelin Loss and Axonal Ion Channel Adaptations Associated with Gray Matter Neuronal Hyperexcitability. J Neurosci 35:7272–7286.

Hanemaaijer NAK, Popovic MA, Wilders X, Grasman S, Arocas OP, Kole MHP (2020) Ca2+ entry through nav channels generates submillisecond axonal ca2+ signaling. Elife 9:1--75.

Holman SP, Lobo AS, Novorolsky RJ, Nichols M, Fiander MDJ, Konda P, Kennedy BE, Gujar S, Robertson GS (2020) Neuronal mitochondrial calcium uniporter deficiency exacerbates axonal injury and suppresses remyelination in mice subjected to experimental autoimmune encephalomyelitis. Exp Neurol 333:113430.

Hu H, Gan J, Jonas P (2014) Fast-spiking, parvalbumin$^{+}$ GABAergic interneurons: From cellular design to microcircuit function. Science 345:1255263.

Hu H, Roth FC, Vandael D, Jonas P (2018) Complementary Tuning of Na+ and K+ Channel Gating Underlies Fast and Energy-Efficient Action Potentials in GABAergic Interneuron Axons. Neuron 98:156-165.e6.

45 Kageyama GH, Wong-Riley MTT (1982) Histochemical localization of cytochrome oxidase in
46 the hippocampus: Correlation with specific neuronal types and afferent pathways.
47 Neuroscience 7:2337–2361.

48 Kann O, Papageorgiou IE, Draguhn A (2014) Highly Energized Inhibitory Interneurons are a
49 Central Element for Information Processing in Cortical Networks. J Cereb Blood Flow
50 Metabolism 34:1270–1282.

51 Kasthuri N et al. (2015) Saturated Reconstruction of a Volume of Neocortex. Cell 162:648–661.

52 Kepecs A, Fishell G (2014) Interneuron cell types are fit to function. Nature 505:318--26
53 Available at: http://www.ncbi.nlm.nih.gov/pubmed/24429630.

54 Kipp M, Clarner T, Dang J, Copray S, Beyer C (2009) The cuprizone animal model: new insights
55 into an old story. Acta Neuropathol 118:723–736.

56 Kiryu-Seo S, Ohno N, Kidd GJ, Komuro H, Trapp BD (2010) Demyelination increases axonal
57 stationary mitochondrial size and the speed of axonal mitochondrial transport. J Neurosci
58 30:6658--66 Available at: http://www.ncbi.nlm.nih.gov/pubmed/20463228
59 http://www.pubmedcentral.nih.gov/articlerender.fcgi?artid=PMC2885867.

60 Kole MH, Brette R (2018) The electrical significance of axon location diversity. Curr Opin
61 Neurobiol 51:52–59.

62 Kole MHP, Letzkus JJ, Stuart GJ (2007) Axon Initial Segment Kv1 Channels Control Axonal
63 Action Potential Waveform and Synaptic Efficacy. Neuron 55:633–647.

64 Kontou G, Antonoudiou P, Podpolny M, Szulc BR, Arancibia-Carcamo IL, Higgs NF, Lopez-
65 Domenech G, Salinas PC, Mann E, Kittler JT (2021) Miro1-dependent mitochondrial
66 dynamics in parvalbumin Interneurons. Elife 10:e65215.

67 Lee Y, Morrison BM, Li Y, Lengacher S, Farah MH, Hoffman PN, Liu Y, Tsingalia A, Jin L,
68 Zhang P-W, Pellerin L, Magistretti PJ, Rothstein JD (2012) Oligodendroglia metabolically
69 support axons and contribute to neurodegeneration. Nature 487:443–448.

70 Lewis TL, Kwon S-K, Lee A, Shaw R, Polleux F (2018) MFF-dependent mitochondrial fission
71 regulates presynaptic release and axon branching by limiting axonal mitochondria size. Nat
72 Commun 9:5008.

73 Li T, Tian C, Scalmani P, Frassoni C, Mantegazza M, Wang Y, Yang M, Wu S, Shu Y (2014)
74 Action Potential Initiation in Neocortical Inhibitory Interneurons Bacci A, ed. Plos Biol
75 12:e1001944 Available at: https://dx.plos.org/10.1371/journal.pbio.1001944.

76 Licht-Mayer S et al. (2020) Enhanced axonal response of mitochondria to demyelination offers
77 neuroprotection: implications for multiple sclerosis. Acta Neuropathol 140:143–167.

78 Mahad DJ, Ziabreva I, Campbell G, Lax N, White K, Hanson PS, Lassmann H, Turnbull DM
79 (2009) Mitochondrial changes within axons in multiple sclerosis. Brain 132:1161–1174.

80 Mazuir E, Fricker D, Sol-Foulon N (2021) Neuron–Oligodendrocyte Communication in
81 Myelination of Cortical GABAergic Cells. Life 11:216.

82 Mensch S, Baraban M, Almeida R, Czopka T, Ausborn J, Manira AE, Lyons DA (2015) Synaptic
83 vesicle release regulates myelin sheath number of individual oligodendrocytes in vivo. Nat
84 Neurosci 18:628–630.

85 Meyer HS, Schwarz D, Wimmer VC, Schmitt AC, Kerr JND, Sakmann B, Helmstaedter M
86 (2011) Inhibitory interneurons in a cortical column form hot zones of inhibition in layers 2 and
87 5A. Proc National Acad Sci 108:16807--12 Available at:
88 http://www.pubmedcentral.nih.gov/articlerender.fcgi?artid=3189020tool=pmcentrezrendertype
89 =abstract.

90 Micheva KD, Chang EF, Nana AL, Seeley WW, Ting JT, Cobbs C, Lein E, Smith SJ, Weinberg
91 RJ, Madison DV (2018) Distinctive Structural and Molecular Features of Myelinated
92 Inhibitory Axons in Human Neocortex. Eneuro 5:ENEURO.0297-18.2018.

93 Micheva KD, Kiraly M, Perez MM, Madison DV (2021) Conduction Velocity Along the Local
94 Axons of Parvalbumin Interneurons Correlates With the Degree of Axonal Myelination. Cereb
95 Cortex 31:bhab018-.

96 Micheva KD, Wolman D, Mensh BD, Pax E, Buchanan J, Smith SJ, Bock DD (2016) A large
97 fraction of neocortical myelin ensheathes axons of local inhibitory neurons. Elife 5:e15784.

98 Mironov SL (2007) ADP Regulates Movements of Mitochondria in Neurons. Biophys J 92:2944–
99 2952.

00 Nave K-A, Werner HB (2014) Myelination of the Nervous System: Mechanisms and Functions.
01 Annu Rev Cell Dev Bi 30:503--533.

02 Nikic I, Merkler D, Sorbara C, Brinkoetter M, Kreutzfeldt M, Bareyre FM, Bruck W, Bishop D,
03 Misgeld T, Kerschensteiner M (2011) A reversible form of axon damage in experimental
04 autoimmune encephalomyelitis and multiple sclerosis. Nat Med 17:495--499 Available at:
05 http://www.ncbi.nlm.nih.gov/pubmed/21441916 http://www.nature.com/articles/nm.2324.

06 Ohno N, Chiang H, Mahad DJ, Kidd GJ, Liu L, Ransohoff RM, Sheng Z-H, Komuro H, Trapp
07 BD (2014) Mitochondrial immobilization mediated by syntaphilin facilitates survival of
08 demyelinated axons. Proc National Acad Sci 111:9953–9958.

09 Ohno N, Kidd GJ, Mahad D, Kiryu-Seo S, Avishai A, Komuro H, Trapp BD (2011) Myelination
10 and Axonal Electrical Activity Modulate the Distribution and Motility of Mitochondria at CNS
11 Nodes of Ranvier. J Neurosci 31:7249–7258.

12 Pekkurnaz G, Trinidad JC, Wang X, Kong D, Schwarz TL (2014) Glucose Regulates
13 Mitochondrial Motility via Milton Modification by O-GlcNAc Transferase. Cell 158:54–68.

14 Philips T, Mironova YA, Jouroukhin Y, Chew J, Vidensky S, Farah MH, Pletnikov MV, Bergles
15 DE, Morrison BM, Rothstein JD (2021) MCT1 Deletion in Oligodendrocyte Lineage Cells
16 Causes Late-Onset Hypomyelination and Axonal Degeneration. Cell Reports 34:108610.

17 Ramaglia V, Dubey M, Malpede MA, Petersen N, Vries SI de, Ahmed SM, Lee DSW, Schenk
18 GJ, Gold SM, Huitinga I, Gommerman JL, Geurts JJG, Kole MHP (2021) Complement-
19 associated loss of CA2 inhibitory synapses in the demyelinated hippocampus impairs memory.
20 Acta Neuropathol 142:643–667.

21 Rangaraju V, Calloway N, Ryan TA (2014) Activity-Driven Local ATP Synthesis Is Required for
22 Synaptic Function. Cell 156:825–835.

23 Rizzuto R, Stefani DD, Raffaello A, Mammucari C (2012) Mitochondria as sensors and
24 regulators of calcium signalling. Nat Rev Mol Cell Bio 13:566–578.

25 Smit-Rigter L, Rajendran R, Silva CAP, Spierenburg L, Groeneweg F, Ruimschotel EM,
26 van Versendaal D, van der Togt C, Eysel UT, Heimel JA, Lohmann C, Levelt CN (2016)
27 Mitochondrial Dynamics in Visual Cortex Are Limited In Vivo and Not Affected by Axonal
28 Structural Plasticity. Curr Biol 26:2609–2616.

29 Stedehouder J, Brizee D, Shpak G, Kushner SA (2018) Activity-Dependent Myelination of
30 Parvalbumin Interneurons Mediated by Axonal Morphological Plasticity. J Neurosci 38:3631–
31 3642.

32 Stedehouder J, Brizee D, Slotman JA, Pascual-Garcia M, Leyrer ML, Bouwen BL, Dirven CM,
33 Gao Z, Berson DM, Houtsmuller AB, Kushner SA (2019) Local axonal morphology guides the
34 topography of interneuron myelination in mouse and human neocortex. Elife 8:e48615.

35 Stedehouder J, Couey JJ, Brizee D, Hosseini B, Slotman JA, Dirven CMF, Shpak G, Houtsmuller
36 AB, Kushner SA (2017) Fast-spiking Parvalbumin Interneurons are Frequently Myelinated in
37 the Cerebral Cortex of Mice and Humans. Cereb Cortex 27:5001–5013.

38 Stedehouder J, Kushner SA (2017) Myelination of parvalbumin interneurons: a parsimonious
39 locus of pathophysiological convergence in schizophrenia. Mol Psychiatr 22:4–12.

40 Trevisiol A, Saab AS, Winkler U, Marx G, Imamura H, Möbius W, Kusch K, Nave K-A,
41 Hirrlinger J (2017) Monitoring ATP dynamics in electrically active white matter tracts. Elife
42 6:e24241.

43 Witte ME, Bø L, Rodenburg RJ, Belien JA, Musters R, Hazes T, Wintjes LT, Smeitink JA,
44 Geurts JJ, Vries HED, Valk P van der, Horssen J van (2009) Enhanced number and activity of
45 mitochondria in multiple sclerosis lesions. J Pathology 219:193–204.

46 Witte ME, Schumacher A-M, Mahler CF, Bewersdorf JP, Lehmitz J, Scheiter A, Sánchez P,
47 Williams PR, Griesbeck O, Naumann R, Misgeld T, Kerschensteiner M (2019) Calcium Influx
48 through Plasma-Membrane Nanoruptures Drives Axon Degeneration in a Model of Multiple
49 Sclerosis. Neuron 101:615-624.e5.

50 Yang SM, Michel K, Jokhi V, Nedivi E, Arlotta P (2020) Neuron class-specific responses govern
51 adaptive myelin remodeling in the neocortex. Sci New York N Y 370.

52 Young EA, Fowler CD, Kidd GJ, Chang A, Rudick R, Fisher E, Trapp BD (2008) Imaging
53 correlates of decreased axonal Na+/K+ ATPase in chronic multiple sclerosis lesions. Ann
54 Neurol 63:428–435.

55 Zambonin JL, Zhao C, Ohno N, Campbell GR, Engeham S, Ziabreva I, Schwarz N, Lee SE,
56 Frischer JM, Turnbull DM, Trapp BD, Lassmann H, Franklin RJM, Mahad DJ (2011)
57 Increased mitochondrial content in remyelinated axons: implications for multiple sclerosis.
58 Brain 134:1901–1913.

59 Zhang Z, David G (2016) Stimulation-induced Ca2+ influx at nodes of Ranvier in mouse
60 peripheral motor axons. J Physiology 594:39–57.

61 Zoupi L, Booker SA, Eigel D, Werner C, Kind PC, Spires-Jones TL, Newland B, Williams AC
62 (2021) Selective vulnerability of inhibitory networks in multiple sclerosis. Acta Neuropathol
63 141:415–429.

64

65

**Acknowledgments**

The authors are thankful to Fred de Winter and Joost Verhaagen (NIN–KNAW) for the support for developing and producing the AAV constructs. We thank Christian Lohmann for critical reading of the manuscript and feedback during this research. We thank Diego de Stefani for generously sharing the 4mt-GCaMP6f plasmid with us. We thank Arnoldo Zaldivar Castro for optimizing the immunohistochemistry protocol.

**Funding:**
The Dutch Research Council NWO Vici 865.17.003 (MK)
Erasmus scholarship G ATHINE 01 (MEB)

**Author contributions:**

Conceptualization: MK, KK
Methodology: MK, KK, MEB, BV
Investigation: KK, MEB, BV, NP
Formal analysis, MK, KK, MEB, BV
Visualization: MK, KK
Funding acquisition: MK
Project administration: MK
Supervision: MK, KK
Writing – original draft: KK
Writing – review & editing: MK, KK

**Competing interests:** Authors declare that they have no competing interests